

## Evaluating the Calibration of SN Ia Anchor Datasets with a Bayesian Hierarchical Model

M. CURRIE,<sup>1</sup> D. RUBIN,<sup>1,2</sup> G. ALDERING,<sup>2</sup> S. DEUSTUA,<sup>1</sup> A. FRUCHTER,<sup>1</sup> AND S. PERLMUTTER<sup>2,3</sup>

<sup>1</sup>*Space Telescope Science Institute, 3700 San Martin Drive, Baltimore, MD 21218*

<sup>2</sup>*E.O. Lawrence Berkeley National Laboratory, 1 Cyclotron Rd., Berkeley, CA, 94720*

<sup>3</sup>*Department of Physics, University of California Berkeley, 366 LeConte Hall MC 7300, Berkeley, CA, 94720-7300*

### ABSTRACT

Inter-survey calibration remains an important systematic uncertainty in cosmological studies using type Ia supernova (SNe Ia). Ideally, each survey would measure its system throughputs, for instance with bandpass measurements combined with observations of well-characterized spectrophotometric standard stars; however, many important nearby-SN surveys have not done this. We recalibrate these surveys by tying their tertiary survey stars to Pan-STARRS1  $g$ ,  $r$ , and  $i$ , and SDSS/CSP  $u$ . This improves upon previous recalibration efforts by taking the spatially variable zeropoints of each telescope/camera into account, and applying improved color transformations in the surveys' natural instrumental photometric systems. Our analysis uses a global hierarchical model of the data which produces a covariance matrix of magnitude offsets and bandpass shifts, quantifying and reducing the systematic uncertainties in the calibration. We call our method CROSS-CALIBration with a Uniform Reanalysis (X-CALIBUR). This approach gains not only from a sophisticated analysis, but also from simply tying our calibration to more color calibrators, rather than just the one color calibrator (BD+17°4708) as many previous efforts have done. The results presented here have the potential to help understand and improve calibration uncertainties upcoming SN Ia cosmological analyses.

*Keywords:* methods: statistical, techniques: photometric, cosmology: observations

### 1. INTRODUCTION

By virtue of their standardizable luminosities, type Ia SNe (SNe Ia) serve as distance indicators spanning nearby galaxies through  $z > 2$ . Measured distances to SNe Ia provided the first strong evidence that the expansion of the universe is accelerating (Riess et al. 1998; Perlmutter et al. 1999), most likely driven by a previously undetected energy density (“dark energy”). Two decades later, with larger SN samples and a greater redshift range, SNe Ia (in combination with other cosmological probes) enable precision measurements of the acceleration behavior, and thus the energy density and equation of state of dark energy as a function of time (Suzuki et al. 2012; Betoule et al. 2014; Scolnic et al. 2018; Riess et al. 2018; Abbott et al. 2019).

As the distances to SNe Ia are determined from their apparent magnitudes, all SNe Ia must be placed on a consistent magnitude scale. Realizing this consistency also requires that each filter bandpass be known in order to combine SNe from different redshifts or surveys. (Of course, this bandpass in-

cludes not just the filter, but also atmosphere, telescope and instrumental optics, and detectors.) The uncertainties in these quantities translate directly to systematic uncertainties on the SN distances. Indeed, photometric calibration is a major systematic uncertainty in the final cosmology analyses (Suzuki et al. 2012; Betoule et al. 2014; Scolnic et al. 2018; Brout et al. 2019).

SNe Ia surveys use similar calibration strategies: see Harris et al. (1981) for a detailed review of the basic technique. On photometric nights, standard star observations (typically of Landolt 1992 or Smith et al. 2002 fields) are interwoven with supernova fields enabling the calibration of the field stars (“tertiary” standards) in the natural photometric system of the survey (the photometric system without any color transformations). These tertiary standards are then used to calibrate the supernovae on both photometric and non-photometric nights. Because absorption by clouds is close to gray (Burke et al. 2010; Buton et al. 2013), i.e., their effect is to change the sensitivity, but not the relative throughput as a function of wavelength, the same procedure works for non-photometric nights, but with a different zeropoint for each frame on such nights.

This procedure leads to heterogeneity, as each survey controls for the various effects differently. Most modern surveys

measure the telescope bandpasses with calibrated monochromatic light (Stubbs et al. 2010; Stritzinger et al. 2011; Hicken et al. 2012), while others attempt to reconstruct their bandpasses by observing spectrophotometric standards with a range of colors (Stritzinger et al. 2002; Jha et al. 2006; Kowalski et al. 2008; Ganeshalingam et al. 2010). In addition, other effects, like heterogeneity over the field of view, are controlled at different levels by different groups, complicating comparisons and adding more uncertainty.

Scolnic et al. (2015) (hereafter S15) sought to test and improve the original calibrations of SN datasets by using the Pan-STARRS1  $3\pi$  survey (Chambers et al. 2016) as an intermediary, rather than relying on Landolt or Smith secondary standards. They named their approach ‘‘Supercal.’’ Pan-STARRS1 covered most of the visible sky from Maui in the  $g_{\text{PS1}}$ ,  $r_{\text{PS1}}$ ,  $i_{\text{PS1}}$ ,  $z_{\text{PS1}}$ , and  $y_{\text{PS1}}$  filters with high spatial uniformity (better than 0.01 magnitudes, Schlafly et al. 2012).<sup>1</sup> The telescope bandpasses have been measured as a function of wavelength using a combination of monochromatic illumination and standard stars (Stubbs et al. 2010; Tonry et al. 2012). This combination of factors makes Pan-STARRS1 uniquely able to calibrate any supernova field visible from the northern hemisphere. Performing this analysis, S15 found good consistency with the original calibrations, except for the  $B$ -band in two datasets (taken with the same camera).

Our goal in this work is to revisit the calibration of the primary nearby SN datasets, taking a different approach than S15 to place all surveys on the same magnitude system. We refer to our result as the CROSS-CALIBRATION with a Uniform Reanalysis (X-CALIBUR). X-CALIBUR quantifies both statistical and systematic uncertainty. In Section 2, we describe X-CALIBUR in detail and the improvements it offers. Section 3 compares our results to the original calibrations and S15. In Section 4, we summarize our main findings and the future directions for this work. In Appendix A, we describe the details of each dataset. Appendix B compares PSF and aperture photometry in PS1, and discuss the differences. Finally, Appendix C updates the SDSS DR15 and PS1 AB offsets.

## 2. CALIBRATION METHODS

We now briefly summarize the S15 Supercal process before explaining how our analysis is different. For S15’s primary analysis, S15 selected tertiary stars and spectrophotometric stellar templates with  $0.35 < g_{\text{PS1}} - i_{\text{PS1}} < 0.55$ . They fit linear color-color relations, where the ordinate was the offset between the survey to be calibrated and a similar Pan-STARRS1 filter, and the abscissa spanned a broad baseline in wavelength (e.g.,  $g_{\text{PS1}} - i_{\text{PS1}}$ ). After fitting the same relation to synthetic photometry of their templates, the off-

sets between the synthesized relation and observed relation were used to bring each SN sample onto the Pan-STARRS1 system. To be specific about the sign, they computed the adjustment that one *adds* to the original system magnitudes to bring them onto the Pan-STARRS1 system (the opposite sign from e.g., Betoule et al. 2013). The primary analysis assumed all bandpasses were known; as discussed in the introduction, most surveys did not measure their bandpasses. An alternative analysis (limited by the sparse color sampling of their primary library) examined the range of colors  $0.35 < g_{\text{PS1}} - i_{\text{PS1}} < 1.0$  (but still used linear transformations, even over this broad color range) to find bandpass shifts (we discuss bandpass shifts in Section 2.3).

Our refined method improves on S15 in four ways. First, we use improved color-color calibrations. For all filters, we use cubic color-color relations in  $g_{\text{PS1}} - i_{\text{PS1}}$ , allowing us to use a wider range in color ( $g_{\text{PS1}} - i_{\text{PS1}} < 1.5$ , Section 2.1) to better measure bandpass shifts (Section 2.3). We also incorporate a second color,  $u_{\text{SDSS/CSP}} - g_{\text{PS1}}$ , for calibrating  $B$ -band data (Section 2.4.2). Second, we work in the natural system for all stellar observations (color transforming back from the standard-system magnitudes that are quoted, Section 2.2.1). Third, we measure and take into account the spatially variable zeropoint of each camera with a (camera-and-epoch-specific) smoothly varying spline over the focal plane (Section 2.4.3). Finally, we build a global, outlier-robust model of the data, and use informative priors (the parameters for these priors are marginalized over, making a hierarchical model) to better constrain epochs with few stellar observations (Section 2.4.4). This hierarchical model naturally produces estimates of the uncertainties and their correlations. We illustrate an example calibration in Figure 1.

We also have a somewhat different calibration path than S15: we first determine offsets between each of the systems to be calibrated and Pan-STARRS1, then use the Pan-STARRS1 magnitudes of CALSPEC spectrophotometric standard stars (a set of standard stars with spectrophotometric observations made mostly by *HST*<sup>2</sup>) to predict the magnitudes of CALSPEC stars in the system to be calibrated. For example, for calibrating the  $V$  band of a SN dataset, we use tertiary stars in common between the  $V$  of the dataset and  $r_{\text{PS1}}$  to estimate  $V - r_{\text{PS1}}$  for CALSPEC stars. Combined with the  $r_{\text{PS1}}$  magnitudes of these CALSPEC stars, we

<sup>2</sup> In the optical, CALSPEC stars have generally been observed by the Space Telescope Imaging Spectrograph on the *Hubble Space Telescope*. CALSPEC stars are calibrated (up to an overall gray scaling factor for all of CALSPEC) to models of three ‘‘primary’’ white dwarfs: GD153, GD71, and G191B2B. The absolute flux scale of CALSPEC is established using Vega (Bohlin & Gilliland 2004; Bohlin 2007, 2014; Bohlin et al. 2014). CALSPEC observations determine the relative flux scale between different filters, and thus for SN cosmology, allow SNe at from different redshifts or surveys to be placed on the same magnitude scale.

<sup>1</sup> <https://panstarrs.stsci.edu/>

predict the magnitudes of the CALSPEC stars, had they been observed in the  $V$  band. After estimating these  $V$  CALSPEC magnitudes from the tertiaries, we compare to synthesized  $V$  AB magnitudes (this is why we must use a spectrophotometric library), and compute the offset that places the  $V$  data on the AB system.

### 2.1. Data Acquisition and Selection

The datasets to be calibrated are the four Harvard-Smithsonian Center for Astrophysics data releases: CfA1 (Riess et al. 1999), CfA2 (Jha et al. 2006), CfA3 (Hicken et al. 2009), CfA4 (Hicken et al. 2012), and the Carnegie Supernova Project (CSP) data releases: (Contreras et al. 2010; Stritzinger et al. 2011). Each survey is described in more detail in Appendix A. The filters used and the Pan-STARRS1 filters we calibrated each to are listed in Table 1. In short, CfA1 observed with two CCDs (“thick”/“thin”) in  $B$ ,  $V$ ,  $R_C$ , and  $I_C$ . CfA2 observed with AndyCam and 4Shooter in  $U$ ,  $B$ ,  $V$ ,  $R_C$ , and  $I_C$ . CfA3 observed with 4Shooter, Minicam, and Keplercam in  $U$ ,  $B$ ,  $V$ ,  $R_C/r$ , and  $I_C/i$ . CfA4 observed with Keplercam in  $U/u$ ,  $B$ ,  $V$ ,  $r$ , and  $i$ . Finally, CSP observed with Swope in  $u$ ,  $g$ ,  $r$ ,  $i$ ,  $B$ , and  $V$ . We do not calibrate any  $u$  or  $U$  data in our analysis because Pan-STARRS1 does not cover these wavelengths.

#### 2.1.1. Pan-STARRS1 Data

The Pan-STARRS1 data release 2 on the Mikulski Archive for Space Telescopes contains both PSF and aperture photometry. PSF photometry should be optimal for stars (e.g., Stetson 1987); but we use Pan-STARRS1 aperture photometry in our calibration instead. We find the Pan-STARRS1 aperture photometry is more linear in magnitude when compared to other datasets. Furthermore, Pan-STARRS1 photometry shows a color offset between PSF and aperture, and the aperture photometry agrees better with CSP Swope, which, like Pan-STARRS1, has had its bandpasses measured (Stritzinger et al. 2011). (We show comparison plots in Appendix B.) We match stars in a  $9''$  radius between the tertiary stars and Pan-STARRS1; this large radius allows us to reject any matches that contain more than one star (and thus may have suspect photometry).

#### 2.1.2. SDSS $u$ -band Data for Calibrating CfA $B$ -band

For calibrating  $B$  band data, we include a second color,  $u_{\text{SDSS/CSP}} - g_{\text{PS1}}$ , extending the wavelength range to span the  $B$ -band (Section 2.4.2). We use  $u_{\text{SDSS}}$  for the CfA datasets (excluding  $B$ -band observations outside the SDSS footprint). The SDSS  $u$ -band data is better calibrated than the CfA  $U/u$ -band data and the number of stars that SDSS captured in its  $u$ -band is comparable.  $u_{\text{CSP}}$  is used for the CSP  $B$ -band calibration instead of  $u_{\text{SDSS}}$ ;  $u_{\text{CSP}}$  is comparably well calibrated (Mosher et al. 2012) but covers more of the CSP tertiary stars.

### 2.1.3. Magnitude Selection

We find that Pan-STARRS1 aperture photometry is linear when compared against CSP (which has similar filters to Pan-STARRS1), and thus do not apply any magnitude cuts.

### 2.1.4. Color Selection

For the  $B$ -band calibrations, we use stars with  $g_{\text{PS1}} - i_{\text{PS1}} < 1.5$  (thus selecting mid-K stars and hotter). The  $u_{\text{SDSS}}$  filters have red leaks due to vacuum desiccation of the interference coatings, and these leaks introduce camera-column-, time-, and airmass-dependent effects (Doi et al. 2010). Our selection limits the impact of the leak to  $\sim 0.04$  magnitudes, and thus the uncertainty on  $u_{\text{SDSS}}$  to  $\sim 0.01$ . Our fit coefficients show that the impact on the  $B$ -band calibration is  $\sim 10\%$  of this uncertainty, or only  $\sim 1$  mmag.

## 2.2. Data Preprocessing

### 2.2.1. Transformation to the Natural System

Natural-system magnitudes are defined by the following relation for, e.g., the  $V$ -band observation of a star

$$V_{\text{Nat}} = ZP_{V_{\text{Nat}}} - \alpha_{V_{\text{Nat}}} X - 2.5 \log_{10}(C_{\text{obs}}), \quad (1)$$

where  $V_{\text{Nat}}$  is the natural system magnitude,  $ZP_{V_{\text{Nat}}}$  is the zeropoint for the  $V$ -band observation,  $X$  is the airmass,  $\alpha_{V_{\text{Nat}}}$  is the  $V$ -band airmass coefficient, and  $C_{\text{obs}}$  is the observed count rate (photon count rate, for a CCD or other photon-sensitive detector). To determine the zeropoint and relate an instrument’s natural-system photometry to photometry from other instruments, stars are frequently placed on a “standard” system. In practice, this requires observing standard stars with known magnitudes in the standard system over a range in color and observing these standards (or other stars) over a range in airmass to determine the transformation (including zeropoints) and the airmass coefficient (Harris et al. 1981). If the  $V_{\text{Nat}}$  bandpass is similar to the standard-system  $V$  bandpass,<sup>3</sup> then transformations between the natural system and the standard system are linear to good approximation, e.g.,

$$V_{\text{Nat}} - V_{\text{Std}} = \beta_V (B_{\text{Std}} - V_{\text{Std}}); \quad (2)$$

for  $V$ -band data, the standard magnitudes historically used come from Landolt (1992).

Although stars transform simply between modest variations on the standard bandpasses, SNe do not because of their complex and variable spectral energy distributions (e.g., Stritzinger et al. 2002). Thus for precision cosmological

<sup>3</sup> Frequently even the standard-system magnitudes are mildly heterogeneous, so the standard system does not have a single bandpass in all cases. See e.g., the discussion in Regnault et al. (2009) of the Landolt system.

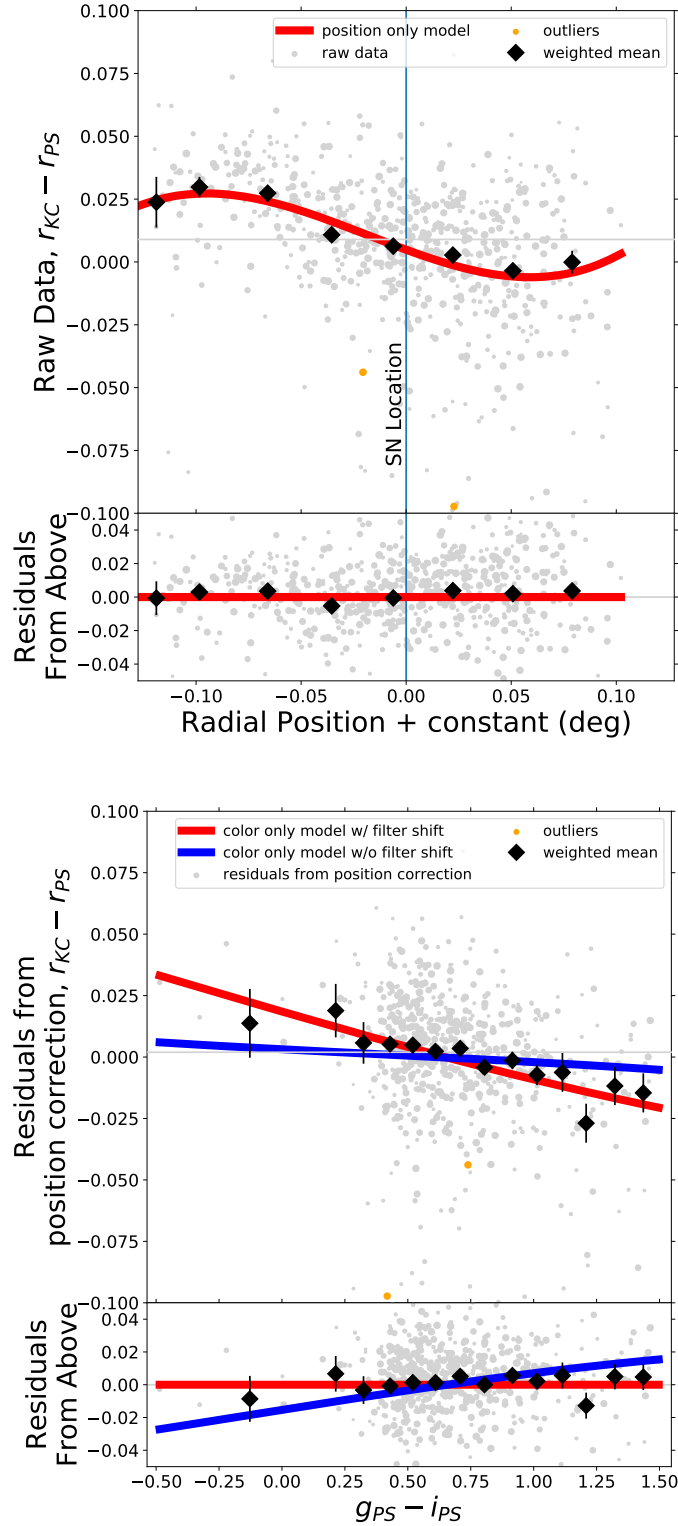


**Figure 1.** Calibration process for the CfA3 Keplercam  $r$  band. All parameters are handled simultaneously in the model, but we show the process as steps for illustrative purposes. The top panel shows the  $r_{KC} - r_{PS1}$  raw data plotted in gray points against radial focal-plane position; larger points indicate magnitudes with smaller uncertainties. A downward-sloping trend is clearly evident (discussed in Section 2.4.3). Removing the spline curve shown in red leaves the residuals in the associated bottom panel. We also show binned weighted-mean values in black for all panels. In the bottom panels, we begin with the residuals from the previous step, and plot these against  $g_{PS1} - i_{PS1}$ . The red line shows the model with the best-fit filter shift ( $\Delta\lambda$ , discussed in Section 2.3), and the blue line shows the model with the original estimate of the filter. A shift of the  $r_{KC}$  filter to the red (positive  $\Delta\lambda$ ) is strongly preferred and is consistently seen in other epochs (Section 3.2). The residuals accounting for both position and color are shown in the associated lower panel.

analyses, working in the natural system is preferred. We thus transform all stellar observations from the standard system (in which they are given) to the natural system by undoing the transformations associated with each dataset, as summarized in Table 3.

### 2.2.2. AB System Offsets for Pan-STARRS1 and $u_{\text{SDSS/CSP}}$

As we observe offsets between PSF and aperture photometry (Appendix B), we compute new CALSPEC AB zero-points for Pan-STARRS1 aperture photometry. We derive these values in Table 4. Table 5 derives corresponding AB offsets for SDSS DR 15. We take 0.06 as the AB offset for CSP/Swope (Krisciunas et al. 2017), where all these offsets are subtracted from the natural-system  $u$  magnitudes to obtain AB magnitudes.

### 2.3. Synthetic Photometry

Empirical color-color relations are sufficient for predicting CALSPEC magnitudes in the natural system of each dataset. However, as the filter bandpasses also play a role in determining SN distances, we solve for these as well. As in S15, we use uniform shifts of size  $\Delta\lambda$  for each filter. Such uniform shifts are adequate for small modifications to the bandpasses, although larger  $\Delta\lambda$  values should be regarded with caution, as different sources of modifications (e.g., blue edge shifts, red edge shifts, and filter leaks) will affect the photometry differently.

The  $\Delta\lambda$  values can only be determined using a synthetic spectral library. We use the INGS spectral library (<https://lco.global/~apickles/INGS/>) for the synthetic photometry for this purpose, as it is better sampled in color and spectral type than CALSPEC.<sup>4</sup> We select only dwarf stars, and for the  $B$  calibrations, we apply the same  $g_{\text{PS1}} - i_{\text{PS1}} < 1.5$  color cut as with the real data. To verify that most of our tertiary stars are dwarfs, we use the handy online implementation <http://model.obs-besancon.fr> for the Robin et al. (2003) model and select similar magnitude and color ranges as the tertiary stars.

### 2.4. Model

For each filter and epoch (see Table 1 for a complete list), the predicted natural-system magnitude minus the corresponding Pan-STARRS1 magnitude for a given star  $j$  is given by

<sup>4</sup> Although CALSPEC has better absolute color calibration, we only need this spectral library to give good internal star-to-star calibration to derive  $\Delta\lambda$  values. The absolute color calibration will largely be absorbed by our use of two different constants ( $\alpha$  and  $\alpha^{\text{Syn}}$ ) in Equations 3 and 4.

$$\begin{aligned}
 m_{\text{Nat } j} - m_{\text{PS } j} = & \alpha + \beta_1[(g_{\text{PS1}} - i_{\text{PS1}})_j - c_1] \\
 & + \beta_2[(g_{\text{PS1}} - i_{\text{PS1}})_j - c_1]^2 \\
 & + \beta_3[(g_{\text{PS1}} - i_{\text{PS1}})_j - c_1]^3 \\
 & + \beta_4[(u_{\text{SDSS/CSP}} - g_{\text{PS1}})_j - c_2] \\
 & + \text{Spline}(\Delta\text{RA} \cdot \cos(\text{Dec}), \Delta\text{Dec}), \quad (3)
 \end{aligned}$$

where  $c_1 \equiv \text{median}(g_{\text{PS1}} - i_{\text{PS1}})$  and  $c_2 \equiv \text{median}(u_{\text{SDSS/CSP}} - g_{\text{PS1}})$ . Subtracting  $c_1$  and  $c_2$  helps to reduce parameter correlations. The first three lines represent the third-order polynomial in  $[g_{\text{PS1}} - i_{\text{PS1}}]$ , as described in Section 2.4.1. The fourth line incorporates  $u$ -band data from either SDSS or CSP (depending on the dataset that is being calibrated), but only for the  $B$ -band calibrations (otherwise  $\beta_4 = 0$ , described in Section 2.4.2). Finally, the last line shows the position-dependent spline which describes the position variation in the response of the dataset to be calibrated (Section 2.4.3). (We work internally in Pan-STARRS1 coordinates, although this choice makes no difference in the aggregated analysis.) The  $\alpha$ ,  $\beta$ , and spline parameters are all inferred simultaneously.

For the synthetic data (Section 2.3), we need a corresponding model, where  $j$  now runs over each dwarf star in the template set:

$$\begin{aligned}
 m_{\text{Nat } j}^{\text{Syn}} - m_{\text{PS } j}^{\text{Syn}} = & \alpha^{\text{Syn}} + \beta_1[(g_{\text{PS1}}^{\text{Syn}} - i_{\text{PS1}}^{\text{Syn}})_j - c_1] \\
 & + \beta_2[(g_{\text{PS1}}^{\text{Syn}} - i_{\text{PS1}}^{\text{Syn}})_j - c_1]^2 \\
 & + \beta_3[(g_{\text{PS1}}^{\text{Syn}} - i_{\text{PS1}}^{\text{Syn}})_j - c_1]^3 \\
 & + \beta_4[(u_{\text{SDSS/CSP}}^{\text{Syn}} - g_{\text{PS1}}^{\text{Syn}})_j - c_2] \\
 & + \frac{\partial m_{\text{Syn } j}}{\partial \Delta\lambda} \Delta\lambda. \quad (4)
 \end{aligned}$$

The first four lines represent the third-order polynomial in  $[g_{\text{PS1}}^{\text{Syn}} - i_{\text{PS1}}^{\text{Syn}}]$  with a linear contribution from  $[u_{\text{SDSS/CSP}}^{\text{Syn}} - g_{\text{PS1}}^{\text{Syn}}]$ , echoing those lines in Equation 3. The final line describes how the synthesized photometry changes when the natural-system bandpass is shifted by an amount  $\Delta\lambda$ . This equation thus enables  $\Delta\lambda$  to be constrained, as it will be adjusted until the synthesized color-color relation matches the observed color-color relation. We further approximate the derivative  $\partial m_{\text{Syn } j} / \partial \Delta\lambda$  with a third-order polynomial (obtained in a separate fit with the nominal bandpass) in  $g_{\text{PS1}} - i_{\text{PS1}}$  (and for calibrating  $B$ , linear in  $u_{\text{SDSS/CSP}} - g_{\text{PS1}}$ ), giving it the same flexibility in color as the synthetic data model.

#### 2.4.1. Color-Color Calibration

For small ranges in color, the offsets between even dissimilar filters (e.g.,  $V$  and  $r$ ) are linear. However, for our broad

color range, we use cubic color-color relations (e.g., Ivezic et al. 2007), as shown in Equations 3 and 4. For simplicity, we use  $g_{\text{PS1}} - i_{\text{PS1}}$  as the primary abscissa color for all calibrations.

#### 2.4.2. *B*-band: Color-Color-Color Calibration

Unlike other color-color relations against Pan-STARRS1, sources of astrophysical variation (e.g. stellar type, extinction, metallicity) have meaningfully different effects in  $B - g_{\text{PS1}}$  as a function of  $g_{\text{PS1}} - i_{\text{PS1}}$ . An example of these effects is shown in Figure 2. We thus find better results calibrating to two colors simultaneously:  $u_{\text{SDSS/CSP}} - g_{\text{PS1}}$  and  $g_{\text{PS1}} - i_{\text{PS1}}$ , transforming an extrapolation ( $B$  is bluer than  $g$ ) into an interpolation ( $B$  sits between  $u$  and  $g$ ). A linear relation is adequate to remove the effects not controlled with  $g_{\text{PS1}} - i_{\text{PS1}}$ , decreasing the residuals, as shown in the bottom panels of Figure 2.

#### 2.4.3. Spatially Variable Response

One of the key assumptions of the S15 analysis is that the tertiary stars and the SNe are on the same magnitude scale. We find the SN observations are always close to the spatial center of the tertiary stars and thus the pointings, while the tertiary stars are distributed throughout the field of view. Thus, one of the ways the same-magnitude-scale assumption might be violated is if the response of the camera (after nominal corrections including flat-fielding and aperture correction) is spatially variable in such a way that the spatially averaged response does not match the response in the center. We find evidence for such spatial variation in the response in most of the tertiary data. An example is illustrated in the middle panel of Figure 3. Here, we show the residuals from the  $B_{\text{KC}} - g_{\text{PS1}}$  calibration binned spatially on the Kepler-cam focal plane. Note that only one corner of the focal plane is used (cf. the top panel of Figure 3). The residuals in the center of the focal plane are fainter (greater than zero), with a clear radial pattern. We see the same radial trend in 4Shooter (used in Cfa2 and Cfa3), and a different trend in CSP. Interestingly, the CSP pattern is not radial, but is a gradient over the focal plane. The size of each trend is summarized in Figure 4.

A likely explanation for these trends, given the large size of the effect (and the time dependence for Kepler-cam), is excess scattered light in the center of the focal plane during the flat-fielding process. I.e., a flat field derived from sky or dome flats would confuse the scattered light for increased efficiency in the center of the field. Without correction using stellar observations (“star flats”), the response will be suppressed in the center of the field (c.f., Regnault et al. 2009). As Kepler-cam is one of the cameras afflicted, and Kepler-cam still exists, this hypothesis could be tested by obtaining scattered-light measurements.

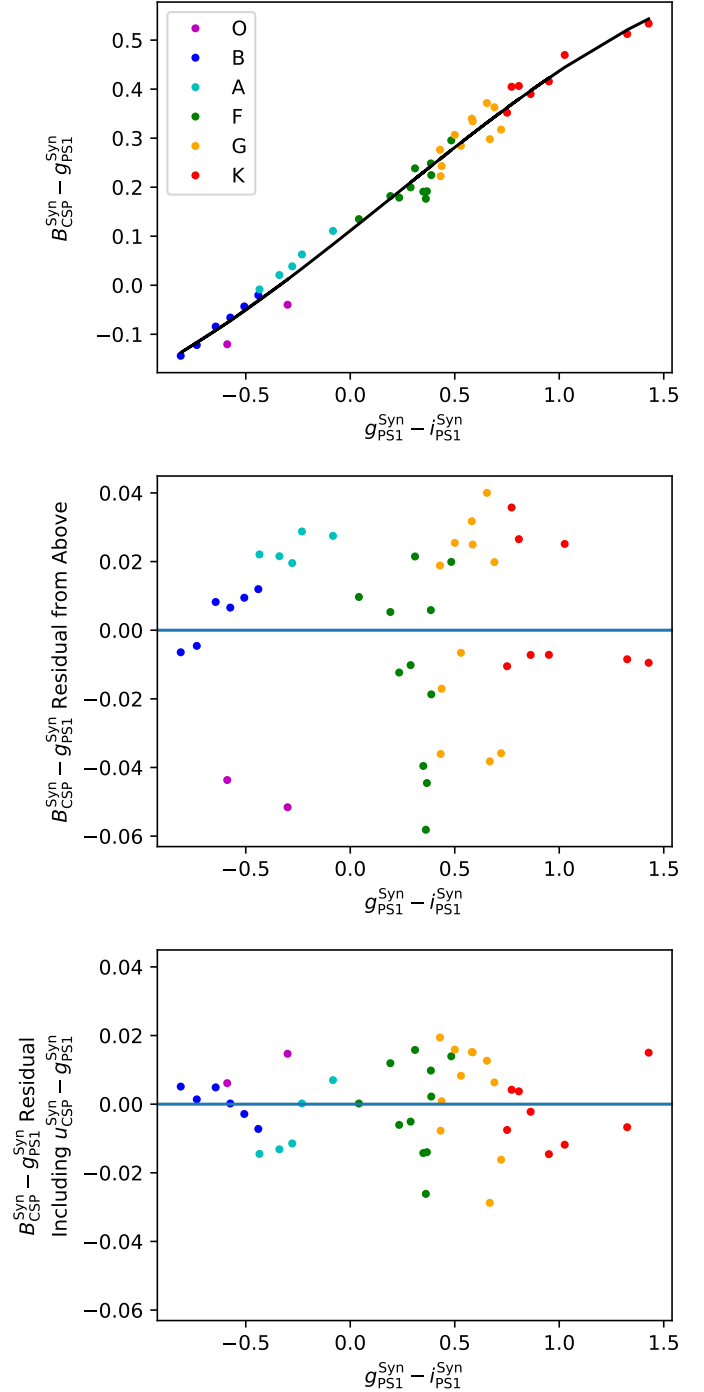


**Figure 2.** Synthesized color-color relations for the dwarf stars in the INGS spectral library showing the importance of incorporating  $u_{\text{CSP}} - g_{\text{PS1}}$  into the  $B_{\text{CSP}} - g_{\text{PS1}}$  calibration. The top panel shows the synthesized color-color relation with its corresponding cubic in  $g_{\text{PS1}}^{\text{Syn}} - i_{\text{PS1}}^{\text{Syn}}$ , color coded by stellar type. The residuals from this relation are shown in the middle panel. The bottom panel shows the residuals when also linearly controlling for the  $u_{\text{CSP}}^{\text{Syn}} - g_{\text{PS1}}^{\text{Syn}}$  color, as in Equation 4. The residuals are substantially improved over the middle panel.

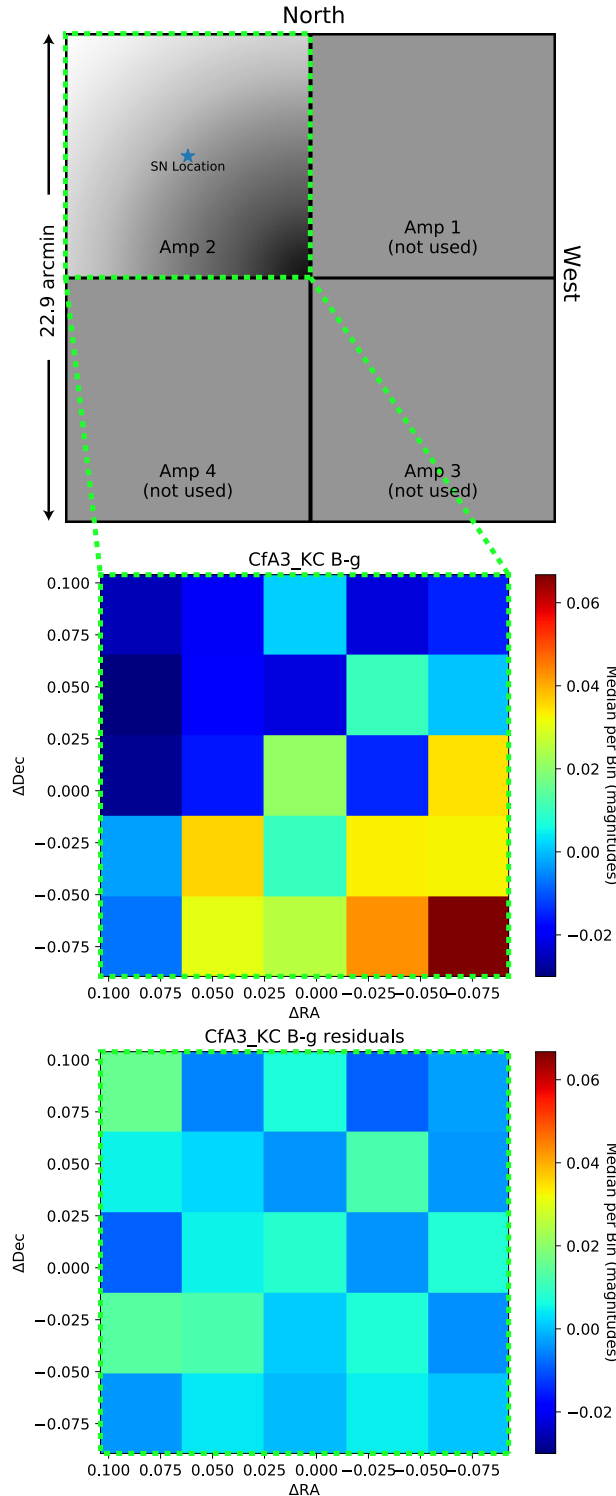


**Figure 3. Top:** Diagram of the KeplerCam CCD camera, used in the CfA3 and CfA4 surveys. The CCD is divided into four 2048-by-2048 quadrants, each read out by a different amplifier. Data were only taken with amplifier 2. For illustrative purposes, the focal plane is shown with a radially varying grayscale over the portion used in the surveys. **Middle:** Median-binned residuals (in magnitudes) in 5-by-5 spatial bins over the corner of the KeplerCam CCD read out by amplifier 2 (for the CfA3 *B*-band data). Positive (fainter) residuals are seen in the lower right corner, while negative residuals are seen along the top and left edges. Comparing to the shading of amplifier 2 in the top panel reveals that this pattern is driven by radial variation (again, only one corner of the KeplerCam CCD was used in the survey). **Bottom:** Residuals after removing our radially varying spline model, described in Section 2.4.3. The spatial trend is accurately removed.

For interference filters, the bandpass shape shifts over the field of view due to variations in field angle. Because these are narrow-field cameras and the bandpass shift changes quadratically with field angle, the effects will be modest. We search for evidence of this by examining residuals for redder and bluer stars separately as a function of position, but see no such evidence. We thus neglect this small effect.

#### 2.4.4. Bayesian Hierarchical Model

There are two further limitations in the data which must be taken into account in the fit. 1) Some epochs have only a limited number of stars (or no stars at all), limiting the accuracy possible. 2) Outliers are present. We address both of these limitations by using a Bayesian hierarchical model that is also robust against outliers. A hierarchical model infers not just parameters, but population distributions of parameters; ours is described below. We sample from our model in Stan (Carpenter et al. 2017) using PyStan (<https://pystan.readthedocs.io>), and make all MCMC samples available on Zenodo.

Our hierarchy includes both sets of calibration parameters: the zeropoints  $\alpha$  and the filter shifts  $\Delta\lambda$ , and uses informative priors on the  $\alpha$  and  $\Delta\lambda$  parameters. These priors are modeled as Gaussian, so there is a mean and dispersion for the  $\alpha$  values, and a mean and dispersion for the  $\Delta\lambda$  values, all of which are marginalized over. The model groups similar calibrations: CfA 1/2/3 4Shooter are modeled together (i.e., there is one set of  $\alpha$  and  $\Delta\lambda$  population parameters for CfA 1/2/3 4Shooter  $B$  band, one for  $V$ , one for  $R$ , and one for  $I$ ), CfA 3 and 4 Keplercam and Minicam together, and CSP together (there is only one filter of each type for CSP, except for  $V$  band, so only  $V$  band is affected by the priors). This hierarchical structure allows the epochs to have different calibrations, but with constraints from other similar calibrations for the epochs that are not as well constrained.

We assume the uncertainties on the  $m_{\text{Nat } i} - m_{\text{PS } i}$  are made up of three components: 1) Statistical uncertainty taken to be the quadrature sum of both the Pan-STARRS1 and the literature natural-system uncertainties. 2) An “unexplained” dispersion, which is parameterized in the model, and also added in quadrature with the uncertainties. 3) Correlations between stars in each field, parameterized with a covariance parameter, assumed to be the same size in each field. As in Rubin et al. (2015), for computational efficiency we implement this covariance by adding nuisance parameters for each field/band that have a prior around zero with variance equal to the covariance (e.g., 0.0001 for (0.01 magnitudes)<sup>2</sup> covariance). Marginalizing over these nuisance parameters is equivalent to adding the covariance to the measurements, but is faster computationally.

As in Krisciunas et al. (2017), we use a two-Gaussian mixture model (one distribution for inliers and one for outliers)

for robustness to outliers. The outlier distribution is centered on the inlier distribution, but has a different width (one parameter for each band). The relative fractions of inliers and outliers are marginalized over, with separate mixture models for the synthetic data and real data. We require the outlier distribution Gaussian to have a width that is at least 0.2 magnitudes, breaking the symmetry between the inlier Gaussian and outlier Gaussian.

### 3. RESULTS

In many cosmology analyses (e.g., Kessler et al. 2009; Conley et al. 2011; Betoule et al. 2014), the natural-system magnitudes of the CALSPEC F8 subdwarf BD+17°4708 are estimated using linear transformations to the Landolt or Smith systems (both Landolt and Smith have measured magnitudes for BD+17°4708). These natural-system magnitudes are used for the calibration of the low redshift datasets in physical units (“fundamental” calibration). There is some evidence that BD+17°4708 may be a variable star (Bohlin & Landolt 2015; Marinoni et al. 2016), making it a poor choice for a standard. For the purposes of comparing against this earlier work, we predict offsets to Pan-STARRS1 for BD+17°4708 in each band to be calibrated. Our results are presented in Table 1 and in Figures 5 through 11; we summarize the key findings for the different surveys here. In Section 3.4, we discuss how much of our changes could be due to the historical choice of BD+17°4708.



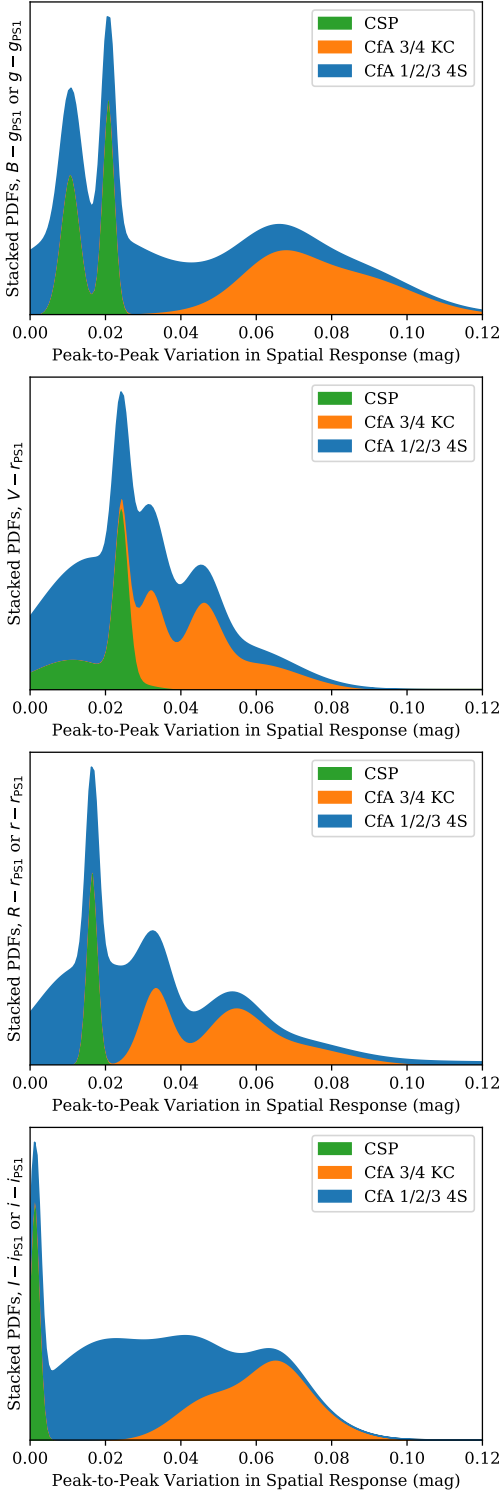


**Figure 4.** Stacked PDFs (one entry for each epoch+filter listed in Table 1) of the peak-to-peak size of the part of the response that depends on focal-plane position (the spline in Section 2.4.3). We color-code by dataset, revealing that the CSP dataset (in green) tends to be at least as well flatfielded as the CfA1, CfA2, and CfA3 4 Shooter dataset (blue), and that the CfA3 and CfA4 Keplercam dataset (orange) is the least well flatfielded (largest peak-to-peak difference with position). Each panel is grouped by wavelength ( $B$  and  $g$ -band data in the top, then  $V$ -band,  $r$  and  $R$  band, and finally  $i$  and  $I$ -band data in the bottom panel); there is no obvious trend with wavelength.

**Table 1.** Summary of X-CALIBUR results. We list each survey and filter in our calibration in the left two columns, then list the Pan-STARRS1 filter that is best matched. The next three columns list the inferred bandpass shift ( $\Delta\lambda$ ), its uncertainty, and the statistical significance (pull) of the bandpass shift. The last three columns list our estimated magnitude offset for BD+17°4708 between the survey/filter we calibrated and the corresponding Pan-STARRS1 filter (e.g.,  $B - g_{\text{PS1}}$  for the first row), its uncertainty, and the estimated BD+17°4708 magnitude when adding this color to the synthesized Pan-STARRS1 magnitude for BD+17°4708 (e.g.,  $[B - g_{\text{PS1}}] + g_{\text{PS1}}^{\text{Syn}}$  for the first row). We must use synthesized photometry for the Pan-STARRS1 magnitudes of BD+17°4708, as it is much too bright to be directly observed with Pan-STARRS1.

Survey	Filt1	Filt2 (PS)	$\Delta\lambda$	$\sigma_{\Delta\lambda}$ (Å)	$\frac{\Delta\lambda}{\sigma_{\Delta\lambda}}$	BD+17 Color	$\sigma_{\text{BD+17Color}}$	BD+17 Mag
CfA1	$B_{\text{thick}}$	$g$	60.7	14.4	4.2	0.3065	0.0144	9.9050
CfA1	$B_{\text{thin}}$	$g$	41.2	18.2	2.3	0.3219	0.0183	9.9204
CfA2	$B_{4\text{Sh1 SAO}}$	$g$	32.4	17.2	1.9	0.3024	0.0129	9.9009
CfA2	$B_{4\text{Sh3 Harris}}$	$g$	42.9	12.7	3.4	0.2965	0.0087	9.8950
CfA2	$B_{4\text{Sh3 SAO}}$	$g$	47.2	25.2	1.9	0.3079	0.0245	9.9064
CfA2	$B_{\text{AC SAO}}$	$g$	34.0	22.5	1.5	0.3062	0.0199	9.9047
CfA2	$B_{\text{AC Harris}}$	$g$	48.2	26.3	1.8	0.2893	0.0268	9.8878
CfA3	$B_{4\text{Sh Harris}}$	$g$	72.7	11.5	6.3	0.2784	0.0055	9.8769
CfA1	$V_{\text{thick}}$	$r$	37.8	10.3	3.7	0.1354	0.0087	9.4938
CfA1	$V_{\text{thin}}$	$r$	42.0	10.9	3.9	0.1289	0.0087	9.4873
CfA2	$V_{4\text{Sh1 SAO}}$	$r$	23.4	14.5	1.6	0.1308	0.0068	9.4892
CfA2	$V_{4\text{Sh3 Harris}}$	$r$	30.5	9.9	3.1	0.1324	0.0045	9.4908
CfA2	$V_{4\text{Sh3 SAO}}$	$r$	33.7	14.9	2.3	0.1253	0.0117	9.4837
CfA2	$V_{\text{AC SAO}}$	$r$	26.5	14.9	1.8	0.1255	0.0096	9.4840
CfA2	$V_{\text{AC Harris}}$	$r$	34.0	15.1	2.2	0.1290	0.0125	9.4874
CfA3	$V_{4\text{Sh Harris}}$	$r$	41.2	8.4	4.9	0.1161	0.0028	9.4745
CfA1	$R_{\text{thick}}$	$r$	22.6	16.1	1.4	-0.1124	0.0101	9.2460
CfA1	$R_{\text{thin}}$	$r$	31.1	17.4	1.8	-0.1244	0.0091	9.2341
CfA2	$R_{4\text{Sh1 SAO}}$	$r$	24.3	16.2	1.5	-0.1549	0.0064	9.2035
CfA2	$R_{4\text{Sh3 Harris}}$	$r$	21.2	15.8	1.3	-0.1820	0.0041	9.1764
CfA2	$R_{4\text{Sh3 SAO}}$	$r$	24.8	18.6	1.3	-0.1515	0.0256	9.2069
CfA2	$R_{\text{AC SAO}}$	$r$	22.8	18.2	1.3	-0.1673	0.0144	9.1911
CfA2	$R_{\text{AC Harris}}$	$r$	24.9	18.7	1.3	-0.1453	0.0435	9.2131
CfA3	$R_{4\text{Sh Harris}}$	$r$	27.6	13.1	2.1	-0.2053	0.0025	9.1531
CfA1	$I_{\text{thick}}$	$i$	31.3	65.7	0.5	-0.4460	0.0144	8.8235
CfA1	$I_{\text{thin}}$	$i$	-1.4	46.6	-0.0	-0.4291	0.0095	8.8403
CfA2	$I_{4\text{Sh1 SAO}}$	$i$	-29.3	50.0	-0.6	-0.4530	0.0089	8.8164
CfA2	$I_{4\text{Sh3 Harris}}$	$i$	-17.5	40.0	-0.4	-0.4096	0.0057	8.8598
CfA2	$I_{4\text{Sh3 SAO}}$	$i$	-21.3	51.1	-0.4	-0.4216	0.0114	8.8479
CfA2	$I_{\text{AC SAO}}$	$i$	-31.3	52.0	-0.6	-0.4437	0.0158	8.8258
CfA2	$I_{\text{AC Harris}}$	$i$	-12.1	51.9	-0.2	-0.4384	0.0276	8.8310
CfA3	$I_{4\text{Sh Harris}}$	$i$	-11.7	32.7	-0.4	-0.4170	0.0033	8.8524
CfA3	$B_{\text{CfA3 KC 1}}$	$g$	14.3	8.8	1.6	0.2867	0.0031	9.8852

**Table 1** continued

Table 1 (continued)

Survey	Filt1	Filt2 (PS)	$\Delta\lambda$	$\sigma_{\Delta\lambda}$ (Å)	$\frac{\Delta\lambda}{\sigma_{\Delta\lambda}}$	BD+17 Color	$\sigma_{\text{BD+17Color}}$	BD+17 Mag
CfA4	$B_{\text{CfA4 KC 1}}$	$g$	23.5	8.8	2.7	0.3003	0.0032	9.8988
CfA4	$B_{\text{CfA4 KC 2}}$	$g$	-42.9	12.1	-3.5	0.2790	0.0061	9.8775
CfA3	$B_{\text{CfA3 MC}}$	$g$	-1.4	46.7	-0.0	0.2734	0.0388	9.8718
CfA3	$V_{\text{CfA3 KC 1}}$	$r$	24.3	6.8	3.6	0.1106	0.0017	9.4690
CfA4	$V_{\text{CfA4 KC 1}}$	$r$	28.0	6.6	4.3	0.1122	0.0018	9.4706
CfA4	$V_{\text{CfA4 KC 2}}$	$r$	36.7	10.5	3.5	0.1162	0.0034	9.4747
CfA3	$V_{\text{CfA3 MC}}$	$r$	29.2	14.8	2.0	0.1130	0.0062	9.4715
CfA3	$r'_{\text{CfA3 KC 1}}$	$r$	61.5	9.7	6.3	0.0069	0.0018	9.3653
CfA4	$r'_{\text{CfA4 KC 1}}$	$r$	77.7	8.0	9.7	0.0042	0.0018	9.3626
CfA4	$r'_{\text{CfA4 KC 2}}$	$r$	74.8	12.4	6.0	0.0144	0.0038	9.3728
CfA3	$r'_{\text{CfA3 MC}}$	$r$	71.2	19.2	3.7	0.0085	0.0112	9.3669
CfA3	$i'_{\text{CfA3 KC 1}}$	$i$	-23.8	15.4	-1.6	-0.0082	0.0017	9.2613
CfA4	$i'_{\text{CfA4 KC 1}}$	$i$	-0.2	14.2	-0.0	-0.0067	0.0017	9.2628
CfA4	$i'_{\text{CfA4 KC 2}}$	$i$	-16.5	18.9	-0.9	-0.0060	0.0029	9.2634
CfA3	$i'_{\text{CfA3 MC}}$	$i$	-13.2	27.4	-0.5	-0.0071	0.0046	9.2624
Swope	$B$	$g$	9.5	11.8	0.8	0.3029	0.0026	9.9013
Swope	$V_{3014}$	$r$	4.9	11.0	0.4	0.1176	0.0042	9.4760
Swope	$V_{9844}$	$r$	19.5	7.6	2.6	0.1084	0.0023	9.4668
Swope	$V_{3009}$	$r$	13.4	25.5	0.5	0.1188	0.0223	9.4772
Swope	$g$	$g$	15.5	4.9	3.2	0.0503	0.0020	9.6487
Swope	$r$	$r$	1.8	5.4	0.3	-0.0064	0.0017	9.3520
Swope	$i$	$i$	-26.6	9.7	-2.7	-0.0272	0.0019	9.2423

### 3.1. CfA1, CfA2, and CfA3 4Shooter

For the CfA1, CfA2, and CfA3 4Shooter data, no measured system throughputs exist. We should therefore not be surprised to find some extreme values for  $\Delta\lambda$ . In Figure 7, we show stacked  $\Delta\lambda$  probability density functions (PDFs) for all datasets and a histogram of pulls of  $\Delta\lambda$  (pull  $\equiv \Delta\lambda/\sigma_{\Delta\lambda}$ ). This figure shows that in absolute terms, the CfA 1/2/3 4Shooter datasets are the most dispersed. Our most extreme results are the large  $\sim -170\text{\AA}$  filter shift in all CfA2 SAO  $I$ -band data, the  $225\text{\AA}$  shift in the CfA1  $R$  for the thin CCD, and the  $\sim 100\text{\AA}$  shift for CfA2 SAO  $R$ -band data. We also see a smaller (but persistent) shift to the red in the  $V$ -band data. For the BD+17°4708 colors, there is a range of compatibility with the original calibrations (shown in Figure 5), but our results and the Landolt-referenced calibration generally agree to within 0.02 magnitudes.

### 3.2. CfA3 and CfA4 Keplercam

Our most extreme result for the bandpasses in CfA3 and CfA4 (Keplercam) is in the  $r$  band, where there is a large, consistent filter shift of  $\sim 70\text{\AA}$ . This shift confirms the tentative conclusion of Amanullah et al. (2010), where a comparison with SDSS  $r$  (Holtzman et al. 2008) showed the CfA3

$r$  band was discrepant. The predicted BD+17°4708 colors agree better with the original calibration than was typical in the previous section, but still show scatter.

An illustration of the benefits of the priors on the calibration parameters (Section 2.4.4) can be found in Figure 8. The three leftmost columns list the estimated magnitude offset from Pan-STARRS1 to Keplercam for CfA3 (leftmost column), CfA4 period 1 (second from the left), and CfA4 period 2 (second from the right). The rightmost column lists the same values for Minicam. Minicam was in use for such a short period of time that no SNe were exclusively observed with it, thus it has no tertiary-star data. The Minicam values thus fall back on the population model, giving values that are similar to the Keplercam measurements, but with much larger and (as shown in Figure 9) less-Gaussian uncertainties. Despite the larger uncertainties, X-CALIBUR still allows Minicam data to be interpreted.

### 3.3. CSP

As expected for data taken with a system that has measured bandpasses, CSP shows the smallest  $\Delta\lambda$  values (all smaller than  $20\text{\AA}$ ). The most statistically significant  $\Delta\lambda$  value is for  $g_{\text{CSP}}$ , with a shift of  $-14.9 \pm 4.5\text{\AA}$ . In Appendix B, we show evidence of a color-dependent offset between PSF and aper-

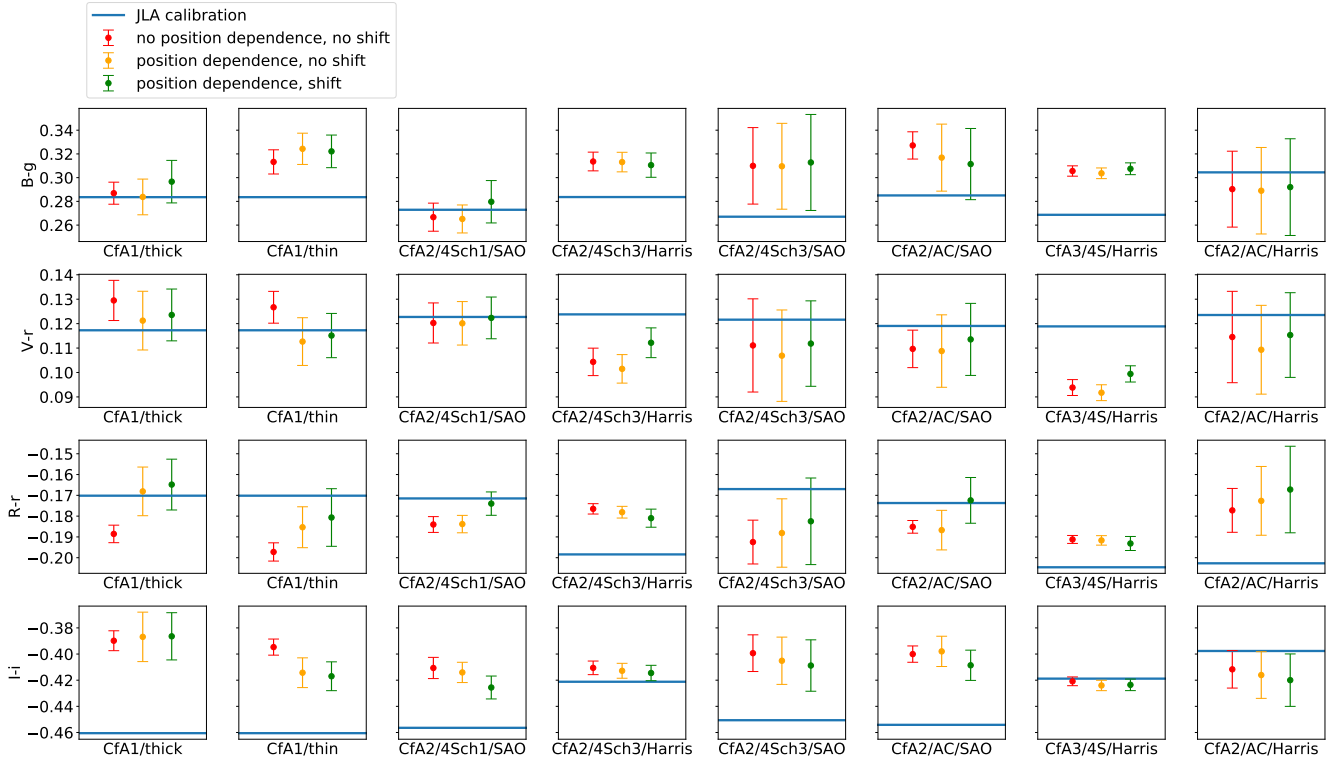


**Figure 5.** BD+17°4708 colors for CfA 1, 2, and 3 (4Shooter). The leftmost measurement in each panel (in red) shows the estimate with no position or color dependence. The next point (yellow) shows the results when the position fit is included; modeling the position dependence generally changes the results by  $< 0.01$  mag, although in some cases the uncertainties can significantly increase. The next point (green) shows the fit with the  $\Delta\lambda$  values included; this is our fiducial analysis. Finally, the horizontal line shows the original JLA calibration.

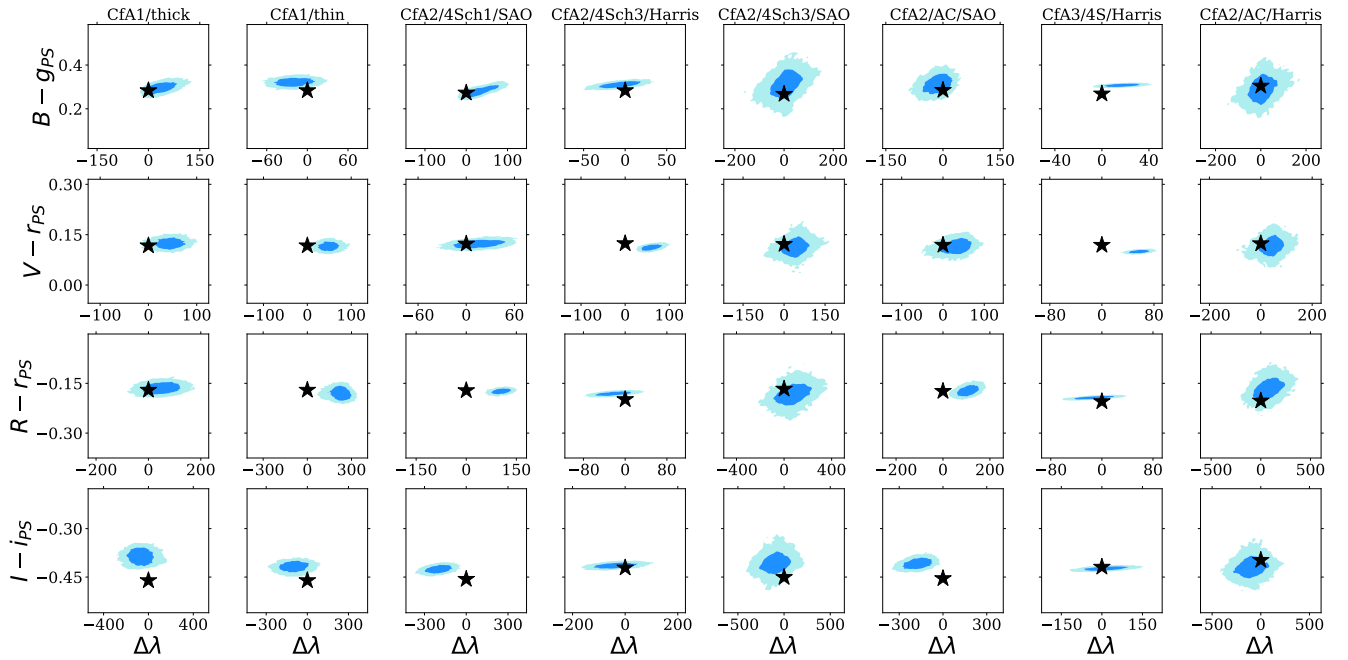


**Figure 6.** Contours showing the 68.3% and 95.4% credible regions for the BD+17°4708 magnitude offset and the filter shift ( $\Delta\lambda$ ) values for each filter/epoch in CfA 1, 2, and 3 (4Shooter). The stars represent the original JLA calibrations.

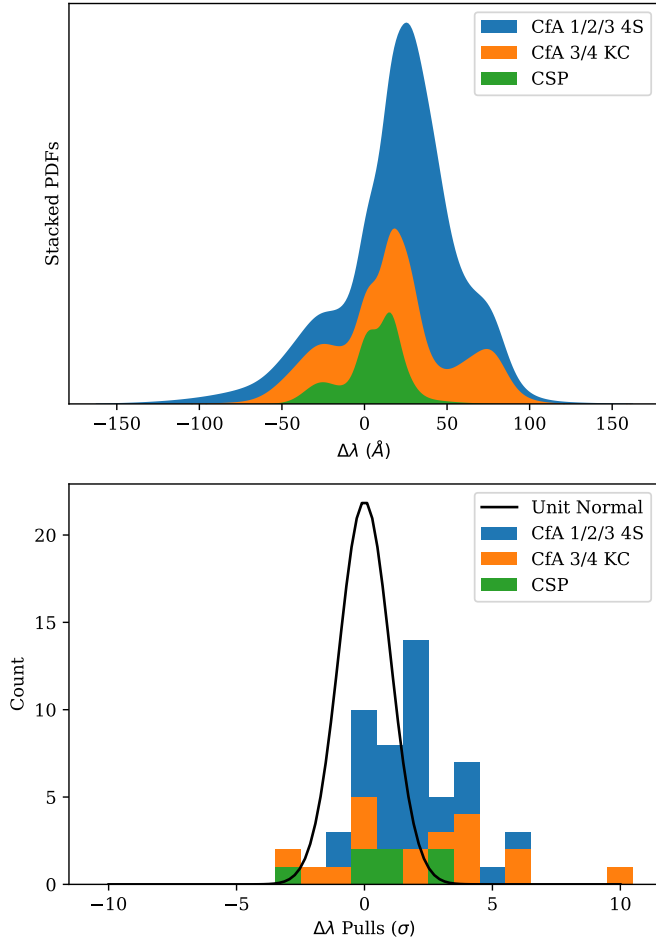


**Figure 7.** Upper panel: stacked PDFs (one for each filter+epoch) for  $\Delta\lambda$ , color coded by dataset, with CfA1, CfA2, and CfA3 4Shooter in blue, CfA3 and CfA4 Keplercam in orange, and CSP in green. The CSP inferred bandpasses agree better with the inputs (narrowest distribution in  $\Delta\lambda$ ). Lower panel: pulls of  $\Delta\lambda$  ( $\equiv \Delta\lambda/\sigma_{\Delta\lambda}$ ). A unit normal is overplotted for reference. The observed distribution is clearly wider than a unit normal, especially for the CfA datasets. This distribution is more extreme than it may appear; as the measurements are from the posterior, the prior (Section 2.4.4) can force the distribution to be narrower than the unit normal.

ture photometry for Pan-STARRS1  $g_{PS1}$  magnitudes. The best agreement with the  $g_{CSP}$  bandpass is with the aperture magnitudes, but this offset could point to issues not yet resolved in the Pan-STARRS1 calibration.

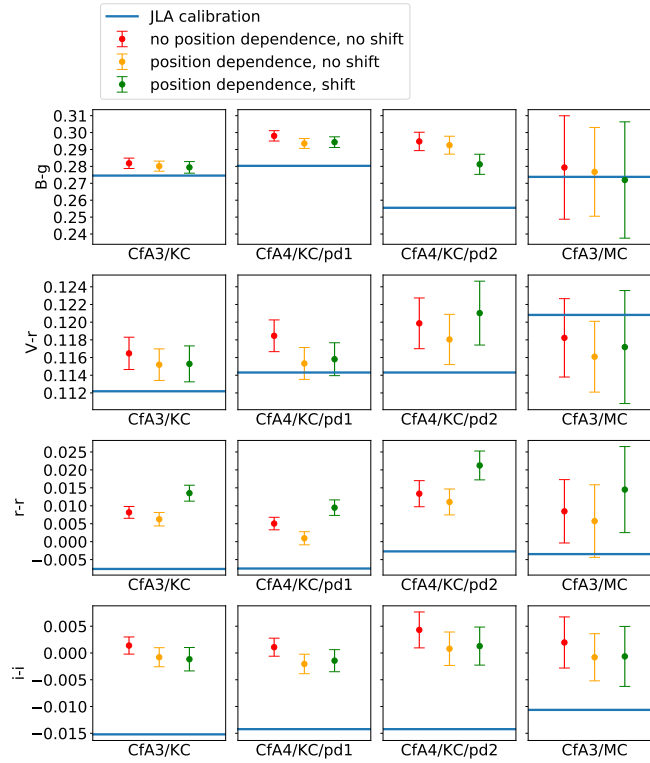


**Figure 8.** BD+17°4708 colors for CfA3 and 4 Keplercam and CfA 3 Minicam. The leftmost measurement in each panel (in red) shows the estimate with no position or color dependence. The next point (yellow) shows the results when the position fit is included. Here, the increase in uncertainty when including the position fit is smaller than for CfA1, CfA2, and CfA3 4Shooter (Figure 6), as there are many more tertiary stars in the analysis. The rightmost point (green) shows the fit with the  $\Delta\lambda$  values included; this is our fiducial analysis. Finally, the horizontal line shows the original JLA calibration.

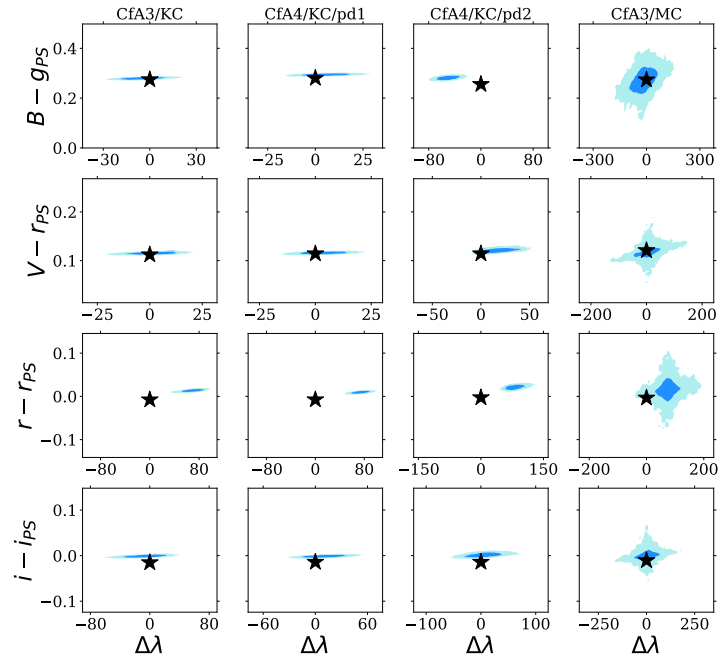


**Figure 9.** Contours showing the 68.3% and 95.4% credible regions for the BD+17°4708 magnitude offset and the filter shift ( $\Delta\lambda$ ) values for each filter/epoch in CfA 3 and 4 Keplercam and CfA 3 Minicam. The stars represent the original JLA calibrations. Our most discrepant finding is a consistent  $r$ -band filter shift for Keplercam (left three panels, second row from bottom).

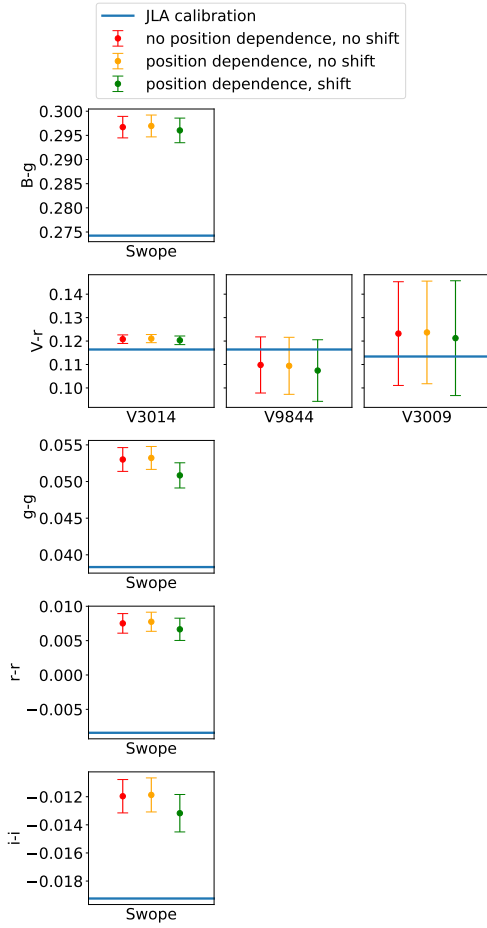


**Figure 10.** BD+17°4708 colors for CSP. The leftmost measurement in each panel (in red) shows the estimate with no position or color dependence. The next point (yellow) shows the results when the position fit is included. The next point (green) shows the fit with the  $\Delta\lambda$  values included; this is our fiducial analysis. Finally, the horizontal line shows the original JLA calibration. The values and uncertainties are consistent across these analyses, indicating that CSP has well-measured bandpasses and that the position dependence of the calibration has little effect.

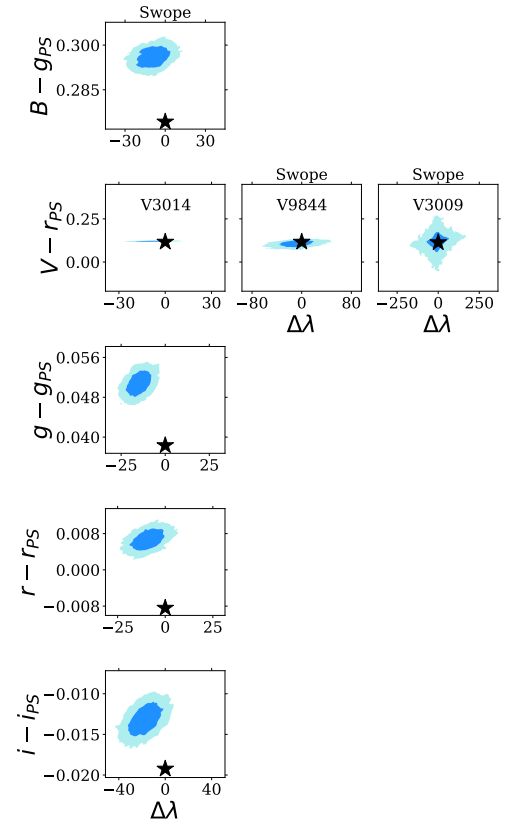


**Figure 11.** Contours showing the 68.3% and 95.4% credible regions for the BD+17°4708 magnitude offset and the filter shift ( $\Delta\lambda$ ) values for each filter/epoch in CSP. The stars represent the original JLA calibrations.



### 3.4. Source of Changes from Previous Calibrations

Some of the calibration differences we observe are due to the arbitrary choice of BD+17°4708 as the SDSS/SNLS3/JLA fundamental standard for low-redshift SNe. As noted in Section 1, the  $g$ ,  $r$ , and  $i$  nearby-SN data was calibrated to Smith et al. (2002) stellar magnitudes. The magnitudes of BD+17°4708 (which was not directly observed by the nearby SN surveys) are then color-transformed to the natural systems and used in the cosmological analyses. But eight other Smith et al. (2002) stars<sup>5</sup> are also in CALSPEC and could be used (individually or together) as references.<sup>6</sup>

To evaluate the impact of choosing any of the other nine CALSPEC stars, and compare the calibration for CSP one derives from Smith et al. (2002) against X-CALIBUR, we conduct the following exercise: 1) We begin by color-transforming all nine stars from Smith et al. (2002) to estimate the  $g_{\text{CSP}}$  magnitudes. 2) We also estimate their  $g_{\text{CSP}}$  magnitudes with X-CALIBUR, i.e., using the tertiary-star color-color relation against Pan-STARRS1 to predict  $g_{\text{CSP}} - g_{\text{PS1}}$  for each star, then estimating the  $g_{\text{PS1}}$  magnitudes using synthetic photometry (as these stars were all too bright to be observed in the Pan-STARRS1 survey) to arrive at estimated  $g_{\text{CSP}}$  magnitudes. We show the distribution of the magnitude differences between these approaches in the top panel of Figure 12. The  $g_{\text{CSP}}$  magnitude difference estimated for BD+17°4708 is 12 mmags, but we find only 4 mmags if we consider the median of the nine. Similarly, the  $r_{\text{CSP}}$  offset drops from 15 mmags to 10 mmags, and the  $i_{\text{CSP}}$  offset drops from 6 mmags to 1 mmag. We show these distributions in the next panels of Figure 12. To conclude, much of the improvement of X-CALIBUR (in the sense that X-CALIBUR is different from a BD+17°4708-referenced calibration) is because of our decision to calibrate to an ensemble of stars, rather than one star.

We can repeat this exercise with Landolt-calibrated data for  $B_{\text{CSP}}$  and  $V_{\text{CSP}}$ . There are four Landolt/CALSPEC stars with colors similar to the bulk of the field stars (which thus have small prediction uncertainties).<sup>7</sup> For  $B_{\text{CSP}}$ , the offset drops from 22 mmags to 2 mmags. For  $V_{\text{CSP}}$ , the offset size is much smaller (4 mmags). It remains constant, but switches sign.<sup>8</sup> Thus for the Landolt-calibrated data as well, much of

the improvement of X-CALIBUR is realized by calibrating to an ensemble of stars.

Thus, to synthesize our AB magnitude offsets, we combine a range of CALSPEC stars. We use dwarf stars, selected to span a similar color range as the tertiaries. We choose two A dwarfs: BD+26°2606 and BD+02°3375, two F dwarfs: BD+29°2091 and BD+21°0607, and two G dwarfs: P330E and P177D.

<sup>5</sup> Six are in Smith et al. (2002); two more are presented in Krisciunas et al. (2017).

<sup>6</sup> The nine stars in common between Smith et al. (2002) and CALSPEC are: BD+21°0607, BD+75°325, BD+54°1216, BD+29°2091, BD+26°2606, BD+02°3375, BD+17°4708, P330E, and P177D.

<sup>7</sup> These four are BD+26°2606, BD+17°4708, P330E, and P177D.

<sup>8</sup> Of course, these offsets are similar to what was seen in Bohlin & Landolt (2015).

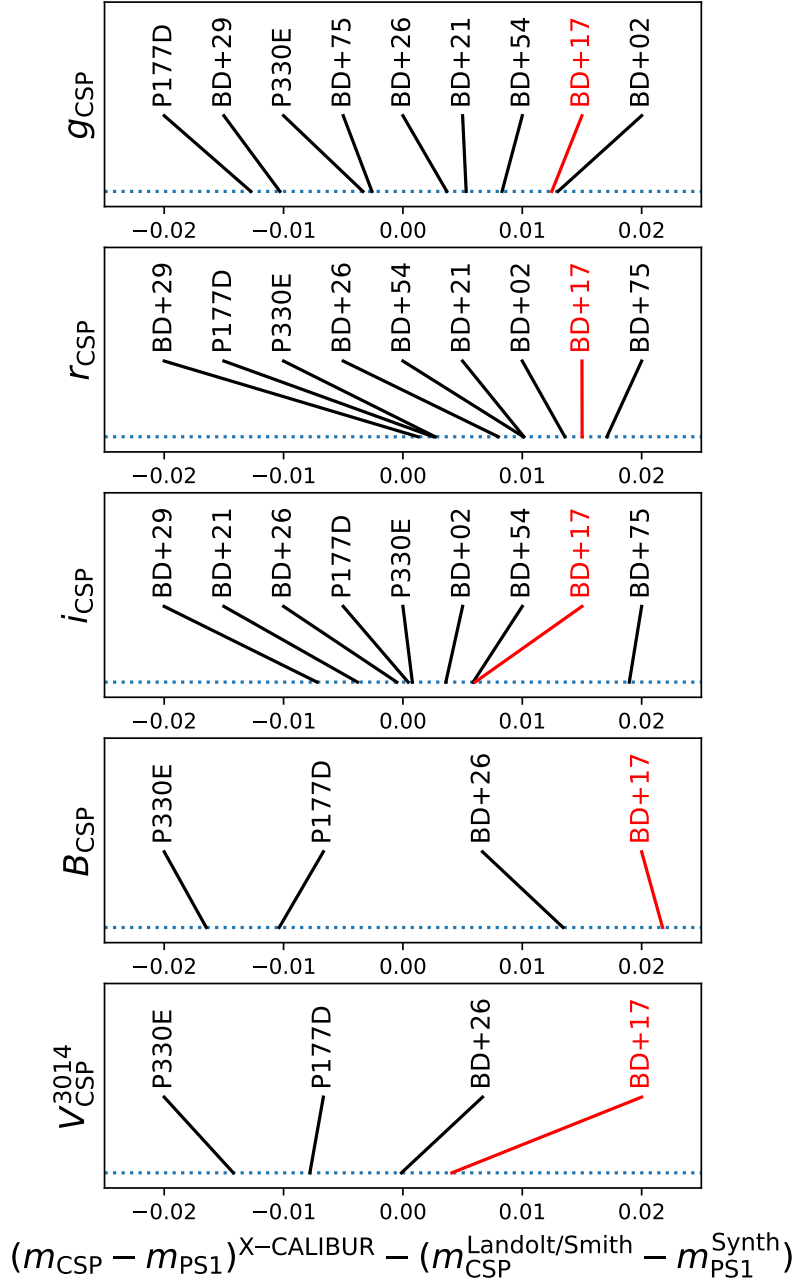


**Figure 12.** Here, we compare the calibration of CSP from X-CALIBUR and the calibration using Landolt/Smith stars. For each star (we discuss the choice of stars in Section 3.4), and each CSP band, we estimate the  $m_{\text{CSP}} - m_{\text{PS1}}$  value from both calibration paths: 1) the X-CALIBUR  $m_{\text{CSP}} - m_{\text{PS1}}$  value estimated using the observed color-color relations of the tertiary stars in common between CSP and Pan-STARRS1. 2) The  $m_{\text{CSP}}^{\text{Landolt/Smith}} - m_{\text{PS1}}^{\text{Synth}}$  value, where  $m_{\text{CSP}}^{\text{Landolt/Smith}}$  is estimated from color-transforming each standard star to the CSP natural system, and  $m_{\text{PS1}}^{\text{Synth}}$  is computed with synthetic photometry (Pan-STARRS1 did not observe these Landolt/Smith stars, as they are too bright). Except for  $r_{\text{CSP}}$ , the average residuals over all stars is very close to zero, and is generally closer to zero than the residuals for BD+17°4708. This indicates that most of the impact X-CALIBUR has (compared to a BD+17°4708-based calibration, such as JLA) on CSP magnitudes is due to averaging over multiple stars.

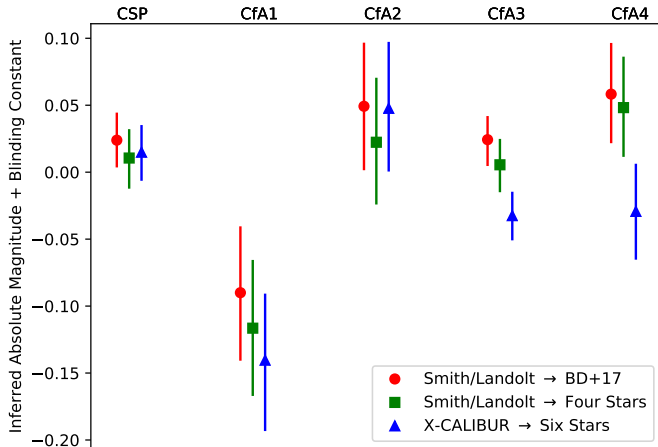


**Figure 13.** Average SN absolute magnitude (up to an additive constant for blinding purposes) for each dataset considered in this work. We show three sets of points: 1) The red (leftmost) dots show the BD+17°4708-referenced calibration. 2) The green (central) squares show the same Smith/Landolt calibration, but calibrated to the average of the six stars discussed in Section 3.4. 3) Finally, the blue (rightmost) triangles show the results using X-CALIBUR. The largest impact of X-CALIBUR is on the Cfa3 and Cfa4 datasets, due to the large  $r$ -band bandpass shift in Keplercam (Section 3.2).

We next compare against S15. We choose the calibration of  $g_{\text{CSP}}$ ,  $r_{\text{CSP}}$ , and  $i_{\text{CSP}}$  for a cross-comparison, as the bandpasses are essentially known and there is little spatial dependence to the CSP/Swope response. We find that we disagree by 3 mmags in  $g$ , 1 mmag in  $r$ , and  $< 1$  mmag in  $i$ . The origin of the larger (but still very small)  $g$  disagreement is not clear, but as discussed in Appendix B,  $g_{\text{PS1}}$  shows the largest offset between aperture and PSF photometry as a function of color. We use aperture photometry, as discussed in Section 3.3, while S15 uses PSF photometry, although not the same PSF photometry as in the Pan-STARRS1 data release (D. Scolnic, private communication). In any case, this gives confidence that, in the limit of little spatial dependence and well understood bandpasses, the S15 analysis and ours give very similar results.

### 3.5. Impact on SN Distances

Finally, we investigate the impact of X-CALIBUR on the nearby-SN Hubble diagram. For each sample of SNe, we compare the BD+17°4708-referenced calibration, the calibration to the average of the four stars discussed in the previous section (still using Smith/Landolt stars as intermediaries), and the full X-CALIBUR calibration. For each of these three calibrations, we fit the light curves with the SALT2 (Guy et al. 2007) light-curve fitter (version 2-4). To compute absolute magnitudes for each SN sample, we take these light-curve fits and feed them into the Unified Inference for Type Ia cosmology (UNITY) framework (Rubin et al. 2015). The UNITY model is modified to infer one

absolute magnitude per sample (instead of one for all samples), and to fix  $\Omega_m$  to 0.3 (these are low-redshift SNe, so our results are insensitive to the exact value of  $\Omega_m$ ). To decrease the uncertainties (but still allow a fair comparison between calibrations), we eliminate the host-mass standardization. UNITY applies this standardization to high-mass-hosted SNe, so there is a large degeneracy with the absolute magnitude, as most of these SNe are from targeted galaxy surveys, and so are hosted by high-mass galaxies. Also to reduce uncertainties, we use linear light-curve-shape and color standardization (Tripp 1998). We use a separate UNITY run for each calibration, then compare the derived absolute magnitudes in Figure 13. We add an arbitrary constant, making it possible to estimate the size of the absolute-magnitude shift between SN samples and between calibrations, while still leaving the implied cosmological result blinded until a future analysis (Rubin et al. in prep.). For CSP, Cfa1, Cfa3, and Cfa4, switching from the BD+17°4708 calibration to the the four-star Landolt/Smith calibration moves the absolute magnitude in the direction of the X-CALIBUR value. This indicates that a fraction of the distance modulus change of X-CALIBUR could have been realized simply by averaging over multiple CALSPEC stars but continuing to use the Landolt/Smith stars as intermediaries.

## 4. SUMMARY

In this work, nearby SN datasets (Cfa1, Cfa2, Cfa3, Cfa4, CSP DR1, and CSP DR2) are calibrated against Pan-STARRS1, rather than the earlier process using Landolt (1992) and Smith et al. (2002) standards. We find a range of agreement with the original calibrations, with some calibration offsets up to several hundredths of a magnitude and bandpass shifts up to  $\sim 200\text{\AA}$ . Improvements on an earlier analysis (Scolnic et al. 2015) are made by: (1) using color-color relations over a wider range in color, allowing us to accurately calibrate filter shifts, (2) incorporating  $u$ -band data into the  $B$ -band calibrations, allowing an interpolation in wavelength, rather than an extrapolation with  $g_{\text{PS1}}$  as the bluest Pan-STARRS1 filter, (3) working only in the natural system for each dataset, (4) presenting evidence for, and a model for removing, spatial variations in the response of the cameras to be calibrated, and (5) building a robust, hierarchical model for the data, making efficient use of filter/camera combinations that have sparse measurements.

### 4.1. Future Work

A future important application of X-CALIBUR will be to Subaru Hyper Suprime-Cam (HSC, Miyazaki et al. 2012). HSC has observed hundreds of distant SNe Ia as part of the Subaru Strategic Program (Aihara et al. 2018), including 23 so far with  $HST$  time (GO 14808 and 15363). It is difficult to image many CALSPEC stars with an 8-meter telescope, so X-CALIBUR will provide the natural intermediary.

This work will also benefit from an improved understanding of the Pan-STARRS1 system and photometry (see Appendix B). In addition, the tie to CALSPEC could be improved by transferring the CALSPEC system to fainter, Pan-STARRS1-observable stars (Narayan et al. 2016b) or (as pointed out in S15) with short exposures of CALSPEC standards (as most of them saturate in the Pan-STARRS1  $3\pi$  survey). We conclude by stressing (as have many others) the general point that bandpasses and standard stars should be measured while the original systems still exist. Both types of measurements should be frequent, and the CALSPEC tie should span as many stars as possible.

#### ACKNOWLEDGMENTS

DR and MC are supported by HST-GO 14808 and 15363, and a NASA *WFIRST* Science Investigation Team. We thank Dan Scolnic and Eddie Schlafly for useful discussions. The Digitized Sky Surveys were produced at the Space Telescope Science Institute under U.S. Government grant NAG W-2166. The images of these surveys are based on photographic data obtained using the Oschin Schmidt Telescope on Palomar Mountain and the UK Schmidt Telescope. The plates were processed into the present compressed digital form with the permission of these institutions.

#### REFERENCES

- Abazajian, K. N., Adelman-McCarthy, J. K., Agüeros, M. A., et al. 2009, *ApJS*, 182, 543
- Abbott, T. M. C., Allam, S., Andersen, P., et al. 2019, *ApJ*, 872, L30
- Aguado, D. S., Ahumada, R., Almeida, A., et al. 2019, *ApJS*, 240, 23
- Aihara, H., Armstrong, R., Bickerton, S., et al. 2018, *PASJ*, 70, S8
- Amanullah, R., Lidman, C., Rubin, D., et al. 2010, *ApJ*, 716, 712
- Bessell, M. S. 1990, *PASP*, 102, 1181
- Betoule, M., Mennier, J., Regnault, N., et al. 2013, *A&A*, 552, A124
- Betoule, M., Kessler, R., Guy, J., et al. 2014, *A&A*, 568, A22
- Bohlin, R. C. 2007, in *Astronomical Society of the Pacific Conference Series*, Vol. 364, *The Future of Photometric, Spectrophotometric and Polarimetric Standardization*, ed. C. Sterken, 315
- Bohlin, R. C. 2014, *AJ*, 147, 127
- Bohlin, R. C., & Gilliland, R. L. 2004, *AJ*, 127, 3508
- Bohlin, R. C., Gordon, K. D., & Tremblay, P. E. 2014, *PASP*, 126, 711
- Bohlin, R. C., & Landolt, A. U. 2015, *AJ*, 149, 122
- Brout, D., Scolnic, D., Kessler, R., et al. 2019, *The Astrophysical Journal*, 874, 150
- Burke, D. L., Axelrod, T., Blondin, S., et al. 2010, *ApJ*, 720, 811
- Buton, C., Copin, Y., Aldering, G., et al. 2013, *A&A*, 549, A8
- Carpenter, B., Gelman, A., Hoffman, M., et al. 2017, *Journal of Statistical Software*, Articles, 76, 1
- Chambers, K. C., Magnier, E. A., Metcalfe, N., et al. 2016, *ArXiv e-prints*, arXiv:1612.05560
- Conley, A., Guy, J., Sullivan, M., et al. 2011, *ApJS*, 192, 1
- Contreras, C., Hamuy, M., Phillips, M. M., et al. 2010, *AJ*, 139, 519
- Doi, M., Tanaka, M., Fukugita, M., et al. 2010, *AJ*, 139, 1628
- Ganeshalingam, M., Li, W., Filippenko, A. V., et al. 2010, *ApJS*, 190, 418
- Guy, J., Astier, P., Baumont, S., et al. 2007, *A&A*, 466, 11
- Harris, W. E., Fitzgerald, M. P., & Reed, B. C. 1981, *PASP*, 93, 507
- Hicken, M., Challis, P., Jha, S., et al. 2009, *ApJ*, 700, 331
- Hicken, M., Challis, P., Kirshner, R. P., et al. 2012, *ApJS*, 200, 12
- Holtzman, J. A., Mennier, J., Kessler, R., et al. 2008, *AJ*, 136, 2306

- Ivezić, Ž., Smith, J. A., Miknaitis, G., et al. 2007, in *Astronomical Society of the Pacific Conference Series*, Vol. 364, *The Future of Photometric, Spectrophotometric and Polarimetric Standardization*, ed. C. Sterken, 165
- Jha, S., Kirshner, R. P., Challis, P., et al. 2006, *AJ*, 131, 527
- Kessler, R., Becker, A. C., Cinabro, D., et al. 2009, *ApJS*, 185, 32
- Kowalski, M., Rubin, D., Aldering, G., et al. 2008, *ApJ*, 686, 749
- Krisciunas, K., Contreras, C., Burns, C. R., et al. 2017, *AJ*, 154, 211
- Landolt, A. U. 1992, *AJ*, 104, 340
- Li, W. D., Filippenko, A. V., Treffers, R. R., et al. 2000, in *American Institute of Physics Conference Series*, Vol. 522, *American Institute of Physics Conference Series*, ed. S. S. Holt & W. W. Zhang, 103–106
- Marinoni, S., Pancino, E., Altavilla, G., et al. 2016, *MNRAS*, 462, 3616
- Miknaitis, G., Pignata, G., Rest, A., et al. 2007, *ApJ*, 666, 674
- Miyazaki, S., Komiyama, Y., Nakaya, H., et al. 2012, in *Proc. SPIE*, Vol. 8446, *Ground-based and Airborne Instrumentation for Astronomy IV*, 84460Z
- Mosher, J., Sako, M., Corlies, L., et al. 2012, *AJ*, 144, 17
- Narayan, G., Rest, A., Tucker, B. E., et al. 2016a, *ApJS*, 224, 3
- Narayan, G., Axelrod, T., Holberg, J. B., et al. 2016b, *ApJ*, 822, 67
- Perlmutter, S., Aldering, G., Goldhaber, G., et al. 1999, *ApJ*, 517, 565
- Regnault, N., Conley, A., Guy, J., et al. 2009, *A&A*, 506, 999
- Riess, A. G., Filippenko, A. V., Challis, P., et al. 1998, *AJ*, 116, 1009
- Riess, A. G., Kirshner, R. P., Schmidt, B. P., et al. 1999, *AJ*, 117, 707
- Riess, A. G., Rodney, S. A., Scolnic, D. M., et al. 2018, *ApJ*, 853, 126
- Robin, A. C., Reylé, C., Derrière, S., & Picaud, S. 2003, *A&A*, 409, 523
- Rubin, D., Aldering, G., Barbary, K., et al. 2015, *ApJ*, 813, 137
- Rubin, D., et al. in prep.
- Sako, M., Bassett, B., Becker, A. C., et al. 2018, *PASP*, 130, 064002
- Schlafly, E. F., Finkbeiner, D. P., Jurić, M., et al. 2012, *ApJ*, 756, 158
- Scolnic, D., Casertano, S., Riess, A., et al. 2015, *ApJ*, 815, 117
- Scolnic, D. M., Jones, D. O., Rest, A., et al. 2018, *ApJ*, 859, 101
- Smith, J. A., Tucker, D. L., Kent, S., et al. 2002, *AJ*, 123, 2121
- Stetson, P. B. 1987, *PASP*, 99, 191
- Stritzinger, M., Hamuy, M., Suntzeff, N. B., et al. 2002, *AJ*, 124, 2100
- Stritzinger, M. D., Phillips, M. M., Boldt, L. N., et al. 2011, *AJ*, 142, 156
- Stubbs, C. W., Doherty, P., Cramer, C., et al. 2010, *ApJS*, 191, 376
- Suzuki, N., Rubin, D., Lidman, C., et al. 2012, *ApJ*, 746, 85
- Tonry, J. L., Stubbs, C. W., Lykke, K. R., et al. 2012, *ApJ*, 750, 99
- Tripp, R. 1998, *A&A*, 331, 815

## APPENDIX

## A. DATASET NOTES

A.1. *CfA1*

The CfA1 (Riess et al. 1999) data release did not provide coordinates for its photometric comparison stars. As a result, we used the labeled postage stamps provided for each SN's field to match the comparison stars with the same field in SDSS SkyServer (for the few targets outside the SDSS footprint, we used the Digitized Sky Survey). Later, we verified our coordinates with A. Riess (private communication) and matched against Pan-STARRS. These coordinates are provided in Table 2. When looking up the comparison stars on SDSS SkyServer, some of the stars originally published have since been reclassified as galaxies. We exclude these from our analysis.

The CfA1 data were taken with the 1.2m telescope at the Fred Lawrence Whipple Observatory (FLWO). Initially, a thick CCD was used to collect the data, but it was later replaced with a thin CCD. This change divides the data into two periods with a dividing line at JD 2449929.5 (or 9929.5 in JD - 2,440,000). As displayed in Table 2, period one (thick CCD) consists of the SNe 1993ac, 1993ae, 1994M, 1994S, 1994T, 1994Q, 1994ae, 1995D, 1995E. Period two (thin CCD) consists of the SNe 1995al, 1995ac, 1995ak, 1995bd, 1996C, 1996X, 1996Z, 1996ab, 1996bl, 1996bo, 1996bk, 1996bv, 1996ai.

The data in CfA1 are presented in the standard system, however for our analysis we convert to the telescope's natural system using the conversion equations in Table 3. We note that the signs are not specified in Riess et al. (1999), but we can infer them by comparing the bandpasses against the Bessell (1990) bandpasses. We note that the  $R$  color terms varied from field-to-field. For the fields the SNe were in, the mean value was not the 0.08 quoted by Riess et al. (1999), but 0.1075 (A. Riess, private communication).

**Table 2.** Stars used in the CfA1 analysis. For each star, we list the SN field it is from, its index in the [Riess et al. \(1999\)](#) analysis, the CCD (thick or thin) used, and its coordinates.

SN	Star Num	CCD	RA (J2000 deg)	Dec (J2000 deg)
1993ac	1	thick	86.59380	63.36620
1993ac	3	thick	86.59194	63.38371
1993ac	4	thick	86.61549	63.36950
1993ae	1	thick	22.44966	-1.96956
1993ae	2	thick	22.41762	-1.94299
1994ae	1	thick	161.71046	17.25359
1994ae	2	thick	161.71130	17.25990
1994ae	3	thick	161.68828	17.31015
1994M	1	thick	187.76020	0.568990
1994M	2	thick	187.76492	0.636890
1994S	1	thick	187.81452	29.16193
1994S	2	thick	187.81720	29.20867
1994S	3	thick	187.77581	29.20676
1994T	1	thick	200.41058	-2.17203
1994T	2	thick	200.42317	-2.19163
1994T	3	thick	200.41947	-2.16481
1994Q	1	thick	252.43958	40.42927
1994Q	2	thick	252.44550	40.41041
1995D	1	thick	145.23116	5.189370
1995D	2	thick	145.17222	5.135190
1995D	4	thick	145.25239	5.184690
1995D	5	thick	145.26143	5.186820
1995E	1	thick	118.02094	73.046892
1995E	2	thick	117.96282	73.039073
1995E	3	thick	117.92352	73.049335
1995E	4	thick	118.2043	73.003885
1995al	1	thin	147.74383	33.55776
1995al	2	thin	147.81630	33.58016
1995al	3	thin	147.68138	33.61648
1995ac	1	thin	341.40928	-8.74144
1995ac	2	thin	341.38925	-8.76661
1995ak	1	thin	41.47188	3.243820
1995ak	2	thin	41.48367	3.266070
1995ak	3	thin	41.40936	3.249240
1995bd	1	thin	71.32829	11.07523
1995bd	2	thin	71.35110	11.10463
1995bd	3	thin	71.37009	11.06579

*Table 2 continued*

**Table 2** (*continued*)

SN	Star Num	CCD	RA (J2000 deg)	Dec (J2000 deg)
1995bd	4	thin	71.30792	11.06381
1996C	1	thin	207.78088	49.31718
1996C	2	thin	207.71994	49.28471
1996C	3	thin	207.64362	49.27640
1996C	4	thin	207.69927	49.31067
1996C	5	thin	207.69423	49.30332
1996X	1	thin	199.54689	-26.806399
1996X	2	thin	199.53797	-26.802915
1996X	3	thin	199.56627	-26.79055
1996X	4	thin	199.58149	-26.826707
1996Z	1	thin	144.19426	-21.174874
1996Z	2	thin	144.15072	-21.098947
1996Z	3	thin	144.16068	-21.089757
1996Z	4	thin	144.15234	-21.082427
1996ab	1	thin	230.26544	27.95686
1996ab	2	thin	230.27389	27.91476
1996ab	4	thin	230.27553	27.94921
1996ab	5	thin	230.30236	27.95619
1996ai	1	thin	197.77806	36.98270
1996ai	2	thin	197.73255	36.99564
1996ai	3	thin	197.79690	37.10335
1996ai	4	thin	197.76008	37.00226
1996ai	5	thin	197.69873	37.01574
1996bk	1	thin	206.71025	60.95914
1996bk	2	thin	206.65837	60.95020
1996bk	3	thin	206.64741	60.99502
1996bl	1	thin	9.043730	11.38184
1996bl	2	thin	9.093120	11.38993
1996bl	3	thin	9.079210	11.36689
1996bl	4	thin	9.039760	11.35679
1996bo	2	thin	27.15455	11.51645
1996bo	3	thin	27.15157	11.47157
1996bo	4	thin	27.14068	11.47326
1996bv	1	thin	94.050928	57.070801
1996bv	2	thin	94.081487	57.036504
1996bv	3	thin	94.101123	57.089443
1996bv	4	thin	94.09153	57.08067

### A.2. CfA2

Due to the many camera/filter combinations, we separate CfA2 (Jha et al. 2006) into four categories: AndyCam/SAO, 4Shooter/SAO (chip1), 4Shooter/SAO (chip 3), and 4Shooter/Harris (chip3). We remove eight SNe that mix different camera+filter combinations: 1998V, 1998dk,

1998dm, 1998dx, 1998ec, 1998ef, 1998es, and 1999X. After removing these mixed combinations, one camera/filter combination had been excluded completely: AndyCam/Harris. As described in Section 2, our hierarchical model still enables a calibration of this combination by virtue of its informative priors.



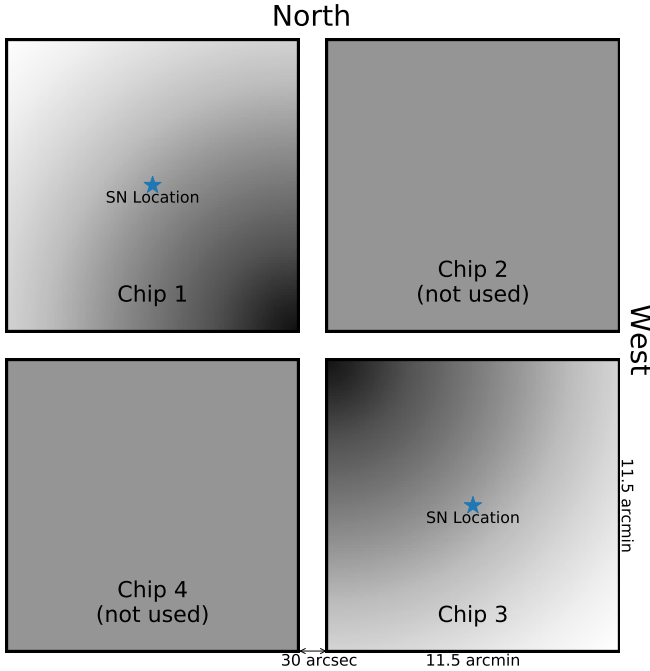


**Figure 14.** Diagram of the 4Shooter CCD camera, used in the CfA2 and CfA3 surveys. The camera is divided into four 2048-by-2048 CCD chips with a 30'' gap between each chip. Data were only taken using chips 1 and 3.

A.3. CfA3

The CfA3 (Hicken et al. 2009) dataset uses two cameras for which we have enough data to calibrate: 4Shooter and

Keplercam. There were five SNe observed with Minicam, which we include with the Keplercam data. Hicken et al. (2009) states that the comparison stars associated with the Minicam SNe were also observed with Minicam, however we find that the distribution of the comparison star locations on the chip is  $\sim 10' \times 10'$ . This matches more closely with the expected Keplercam distribution of  $11.5' \times 11.5'$  rather than the expected  $5.1' \times 23.1'$  Minicam distribution. Therefore, we conclude that the comparison star photometry was taken using Keplercam instead of Minicam and we are able to include these Minicam comparison star data in our Keplercam analysis.

The 4Shooter data were always taken on chip 3 (Figure 14); the KeplerCam data were always taken on amplifier 2 (top panel of Figure 3).

We exclude three SNe from the CfA3 Keplercam dataset due to repeated values in the U-B measurements for the following SNe: 2006em, 2006en, and 2006ke. In the other cases, we use the standard-system photometry, transforming into natural for our analysis.

A.4. CfA4

For CfA4, a small fraction of the SNe are in two periods, representing bandpass changes over time (Hicken et al. 2012). If the vast majority (or all) of the observations are in one period, we assign the SN to that period. If not, we exclude the SN.

A diagram showing the CCD layout is shown in the top panel of Figure 3. The data in this survey were taken using only one corner of the CCD, amplifier 2. We show a radially varying response similar to what is observed in the data.

**Table 3.** Compiled color-color relations for each survey.

Dataset	Camera	Transformation to Natural: Lt = Landolt; Sm = Smith
Riess et al. (1999)	Thick/Thin CCD	$B = B_{Lt} - 0.04 * (B_{Lt} - V_{Lt})$ $V = V_{Lt} + 0.03 * (B_{Lt} - V_{Lt})$ $R = R_{Lt} + 0.1075 * (V_{Lt} - R_{Lt})$ $I = I_{Lt} - 0.06 * (V_{Lt} - I_{Lt})$
Jha et al. (2006)	4Sh-chip1/SAO	$V_{4S} = V_{Lt} + 0.0423 * (B_{Lt} - V_{Lt})$ $U_{4S} - B_{4S} = 0.9433 * (U_{Lt} - B_{Lt})$ $B_{4S} - V_{4S} = 0.8937 * (B_{Lt} - V_{Lt})$ $V_{4S} - R_{4S} = 0.9873 * (V_{Lt} - R_{Lt})$ $V_{4S} - I_{4S} = 1.0837 * (V_{Lt} - I_{Lt})$
Jha et al. (2006)	4Sh-chip3/Harris	$V_{4S} = V_{Lt} + 0.0447 * (B_{Lt} - V_{Lt})$ $U_{4S} - B_{4S} = 0.9638 * (U_{Lt} - B_{Lt})$ $B_{4S} - V_{4S} = 0.9155 * (B_{Lt} - V_{Lt})$

**Table 3 continued**

**Table 3** (continued)

Dataset	Camera	Transformation to Natural: Lt = Landolt; Sm = Smith
		$V_{4S} - R_{4S} = 1.0812 * (V_{Lt} - R_{Lt})$
		$V_{4S} - I_{4S} = 1.0284 * (V_{Lt} - I_{Lt})$
Jha et al. (2006)	4Sh-chip3/Harris+I <sub>SAO</sub>	$V_{4S} - I_{4S} = 1.0900 * (V_{Lt} - I_{Lt})$
Jha et al. (2006)	4Sh-chip3/SAO	$V_{4S} = V_{Lt} + 0.0398 * (B_{Lt} - V_{Lt})$
		$U_{4S} - B_{4S} = 0.9650 * (U_{Lt} - B_{Lt})$
		$B_{4S} - V_{4S} = 0.8830 * (B_{Lt} - V_{Lt})$
		$V_{4S} - R_{4S} = 0.9685 * (V_{Lt} - R_{Lt})$
		$V_{4S} - I_{4S} = 1.0725 * (V_{Lt} - I_{Lt})$
Jha et al. (2006)	AndyCam/Harris	$V_{AC} = V_{Lt} + 0.0441 * (B_{Lt} - V_{Lt})$
		$U_{AC} - B_{AC} = 0.9617 * (U_{Lt} - B_{Lt})$
		$B_{AC} - V_{AC} = 0.9631 * (B_{Lt} - V_{Lt})$
		$V_{AC} - R_{AC} = 1.0947 * (V_{Lt} - R_{Lt})$
		$V_{AC} - I_{AC} = 0.9899 * (V_{Lt} - I_{Lt})$
Jha et al. (2006)	AndyCam/Harris+I <sub>SAO</sub>	$V_{AC} - I_{AC} = 1.0639 * (V_{Lt} - I_{Lt})$
Jha et al. (2006)	AndyCam/SAO	$V_{AC} = V_{Lt} + 0.0340 * (B_{Lt} - V_{Lt})$
		$U_{AC} - B_{AC} = 0.9312 * (U_{Lt} - B_{Lt})$
		$B_{AC} - V_{AC} = 0.9293 * (B_{Lt} - V_{Lt})$
		$V_{AC} - R_{AC} = 0.9824 * (V_{Lt} - R_{Lt})$
		$V_{AC} - I_{AC} = 1.0739 * (V_{Lt} - I_{Lt})$
Hicken et al. (2009)	4Shooter	$U_{4S} - B_{4S} = 0.9912 * (U_{Lt} - B_{Lt})$
		$B_{4S} - V_{4S} = 0.8928 * (B_{Lt} - V_{Lt})$
		$V_{4S} = V_{Lt} + 0.0336 * (B_{Lt} - V_{Lt})$
		$V_{4S} - R_{4S} = 1.0855 * (V_{Lt} - R_{Lt})$
		$V_{4S} - I_{4S} = 1.0166 * (V_{Lt} - I_{Lt})$
Hicken et al. (2009)	Minicam	$U_{MC} - B_{MC} = 1.0060 * (U_{Lt} - B_{Lt})$
		$B_{MC} - V_{MC} = 0.9000 * (B_{Lt} - V_{Lt})$
		$V_{MC} = V_{Lt} + 0.0380 * (B_{Lt} - V_{Lt})$
		$V_{MC} - r_{MC} = 1.0903 * (V_{Lt} - r_{Sm})$
		$V_{MC} - i_{MC} = 1.0375 * (V_{Lt} - i_{Sm})$
Hicken et al. (2009)	Keplercam	$U_{KC} - B_{KC} = 1.0279 * (U_{Lt} - B_{Lt})$
		$B_{KC} - V_{KC} = 0.9212 * (B_{Lt} - V_{Lt})$
		$V_{KC} = V_{Lt} + 0.0185 * (B_{Lt} - V_{Lt})$
		$V_{KC} - r_{KC} = 1.0508 * (V_{Lt} - r_{Sm})$
		$V_{KC} - i_{KC} = 1.0185 * (V_{Lt} - i_{Sm})$
Hicken et al. (2012)	Keplercam (pd.1)	$U_{KC} - B_{KC} = 0.9981 * (U_{Lt} - B_{Lt})$
		$U_{KC} - B_{KC} = 0.9089 * (u_{Sm} - B_{Lt})$
		$B_{KC} - V_{KC} = 0.9294 * (B_{Lt} - V_{Lt})$
		$V_{KC} = V_{Lt} + 0.0233 * (B_{Lt} - V_{Lt})$
		$V_{KC} - r_{KC} = 1.0684 * (V_{Lt} - r_{Sm})$
		$V_{KC} - i_{KC} = 1.0239 * (V_{Lt} - i_{Sm})$
Hicken et al. (2012)	Keplercam (pd.2)	$U_{KC} - B_{KC} = 0.9981 * (U_{Lt} - B_{Lt})$

**Table 3** continued

Table 3 (continued)

Dataset	Camera	Transformation to Natural: Lt = Landolt; Sm = Smith
		$U_{KC} - B_{KC} = 0.9089 * (u_{Sm} - B_{Lt})$
		$B_{KC} - V_{KC} = 0.8734 * (B_{Lt} - V_{Lt})$
		$V_{KC} = V_{Lt} + 0.0233 * (B_{Lt} - V_{Lt})$
		$V_{KC} - r_{KC} = 1.0265 * (V_{Lt} - r_{Sm})$
		$V_{KC} - i_{KC} = 1.0239 * (V_{Lt} - i_{Sm})$
Contreras et al. (2010)	Swope	$B_{CSP} = B_{Lt} - 0.069 * (B_{Lt} - V_{Lt})$
Stritzinger et al. (2011)		$V_{S3014} = V_{Lt} + 0.059 * (V_{Lt} - i_{Sm})$
		$V_{S3009} = V_{Lt} + 0.034 * (V_{Lt} - i_{Sm})$
		$V_{S9844} = V_{Lt} + 0.063 * (V_{Lt} - i_{Sm})$
		$u_{CSP} = u_{Sm} - 0.050 * (u_{Sm} - g_{Sm})$
		$g_{CSP} = g_{Sm} + 0.014 * (g_{Sm} - r_{Sm})$
		$r_{CSP} = r_{Sm} + 0.016 * (r_{Sm} - i_{Sm})$
		$i_{CSP} = i_{Sm}$

### A.5. CSP

The Carnegie Supernova Project (CSP) data used in this analysis are a combination of the first (Contreras et al. 2010) and second (Stritzinger et al. 2011) CSP data releases. The bandpasses in these two datasets remain the same except for the  $V$  band. There were three separate  $V$  filters used:  $V3009$ ,  $V3014$ , and  $V9844$ . Due to overlap in SN observations between the  $V$  filters, ten SNe had to be excluded from the analysis: SN 2005eq, SN 2005hc, SN 2005hj, SN 2005iq, SN 2005ke, SN 2005ki, SN 2005lu, SN 2005mc, SN 2005na, SN 2006D, and SN 2006hx.

Removing the SNe that were observed in mixed filters excludes one of the  $V$  filters completely:  $V3009$ . As noted for AndyCam/Harris, our hierarchical model (described in Section 2) still enables a calibration of this combination (with much larger uncertainties).

We note that in the first CSP data release (Contreras et al. 2010), SN2006ax is mislabeled as SN2006X.

At the time of writing, a third CSP data release became available. However, we leave the analysis of the third data release to future work.

### A.6. Other SN Datasets

The Lick Observatory Supernova Search (LOSS) light-curve data (Ganeshalingam et al. 2010) were primarily taken with the Katzman Automatic Imaging Telescope (KAIT, Li et al. 2000), and thus incorporating them into our analysis might be assumed to be possible. However, most of the magnitudes for the tertiary stars were obtained with the Nickel telescope, then transferred to the SN observations that had been obtained with KAIT. This two-stage process is impossi-

ble to reverse engineer from the published data,<sup>9</sup> so we must exclude the LOSS data from this analysis. For a similar reason, we cannot recalibrate the low-redshift SNe presented in Kowalski et al. (2008).

The tertiary-star data for the Equation of State: Supernovae trace Cosmic Expansion (ESSENCE) survey (Miknaitis et al. 2007; Narayan et al. 2016a) were not presented, so we cannot calibrate this survey.

### B. Pan-STARRS1 PHOTOMETRY

As noted in Section 2.1, we find better agreement (as a function of color and magnitude) between Pan-STARRS1 and other systems when using Pan-STARRS1 aperture photometry rather than PSF photometry. Thus, there must be an offset between aperture and PSF photometry as a function of color and magnitude. Figure 15 shows the difference between aperture and PSF photometry in  $g_{PS1}$ ,  $r_{PS1}$ , and  $i_{PS1}$  as a function of magnitude; a clear trend is visible in all filters. Figure 16 shows these differences as a function of  $g_{PS1} - i_{PS1}$ . A trend in color is visible in  $g_{PS1}$ , with no strong trend in  $r_{PS1}$  and  $i_{PS1}$ . Interestingly,  $g_{CSP}$  shows the most statistically significant filter shift ( $-14.9 \pm 4.5 \text{ \AA}$ ) from the original calibration. It is thus possible that the  $g_{PS1}$  bandpass needs a modest amount of modification.

<sup>9</sup> For example, suppose Nickel has a spatially flat calibration but KAIT does not. Then we would see no spatial variation in the calibration of the tertiary star magnitudes, but the SN photometry could be significantly biased (as the SNe would be calibrated to the field average, which is not the response at the SN location). As another possibility, suppose Nickel has a spatially variable calibration, but KAIT does not. In this case, we would incorrectly calibrate the response to the SN location, when the field average is actually the correct choice.

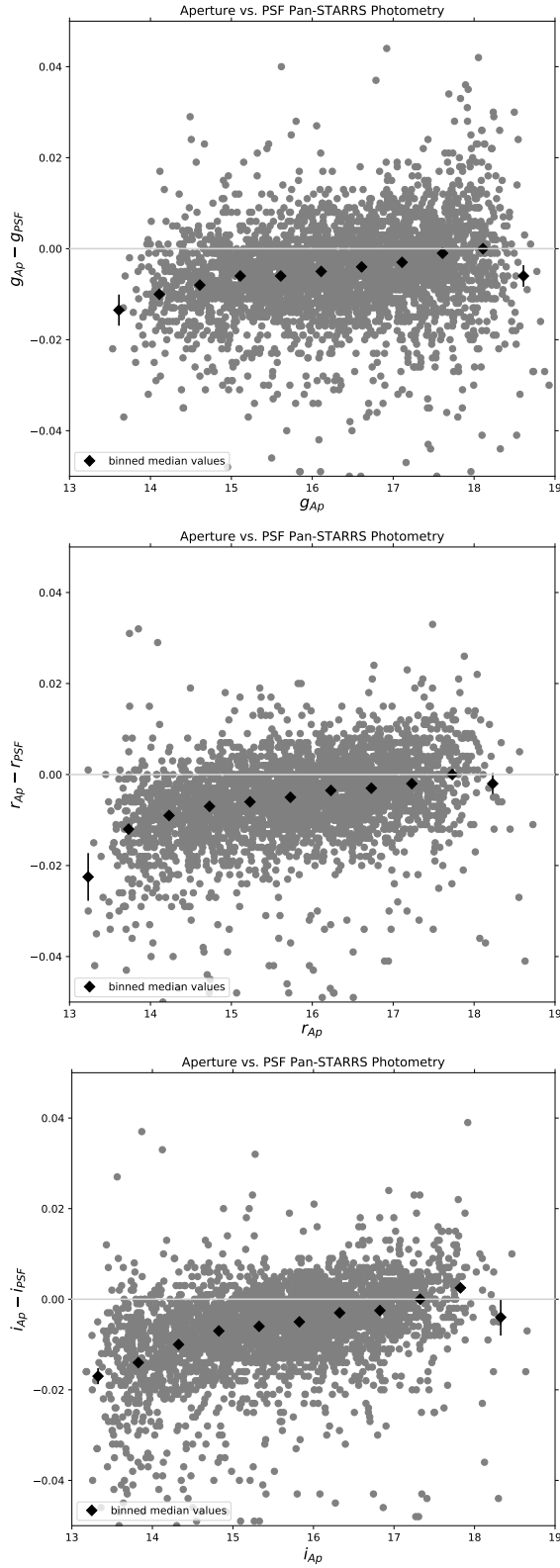


**Figure 15.** Offsets between Pan-STARRS1 aperture and PSF photometry vs. magnitude. The top panel shows  $g_{PS1}$ , the middle panel shows  $r_{PS1}$ , and the bottom panel shows  $i_{PS1}$ . The gray points show the measurements for each star, while the black points are medians in bins. Clear trends are visible; comparison with other datasets indicate that the aperture photometry is more linear.

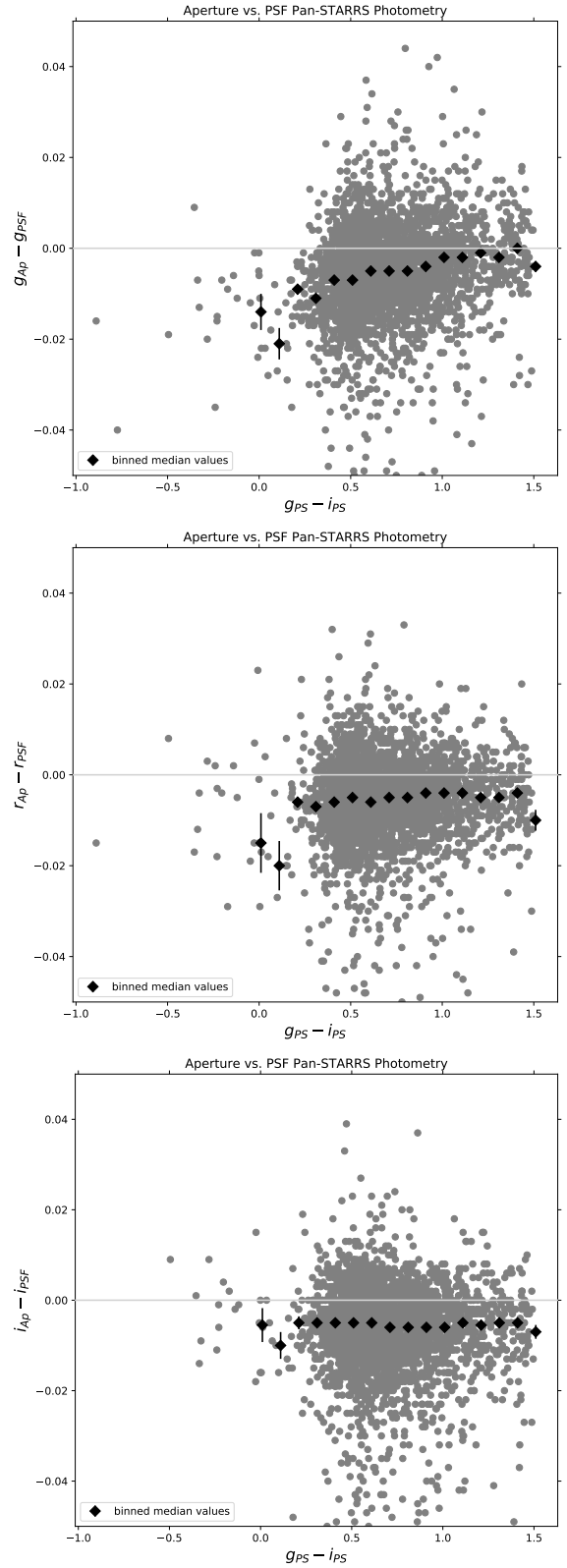


**Figure 16.** Offsets between Pan-STARRS1 aperture and PSF photometry vs. color in Pan-STARRS1  $g_{PS1} - i_{PS1}$ . The top panel shows  $g_{PS1}$ , the middle panel shows  $r_{PS1}$ , and the bottom panel shows  $i_{PS1}$ . The gray points show the measurements for each star, while the black points are medians in bins. A clear trend is visible in the  $g_{PS1}$  data, as well as a weaker trend in  $r_{PS1}$ . Comparison with Swope indicates better agreement with aperture photometry.

### C. SDSS AB OFFSETS

An absolute calibration of the  $u_{\text{SDSS}}$  photometry is necessary for a comparison against synthetic magnitudes. We follow [Betoule et al. \(2013\)](#) in calibrating SDSS to CALSPEC (i.e., computing the SDSS AB offsets) using the 0.5-meter Photometric Telescope (PT) CALSPEC observations as intermediaries. So that they all appear in one place, we compute the AB offsets for each SDSS band (not just  $u$ ). Since [Betoule et al. \(2013\)](#), the following updates have happened, and we must take into account the impact of each.

- The SDSS SN photometry ([Betoule et al. 2014](#); [Sako et al. 2018](#)) is based on data release (DR) 7 ([Abazajian et al. 2009](#)). For the tertiary stars, we use DR15 ([Aguado et al. 2019](#)). As the PT observations are placed on the SN photometric system by [Betoule et al. \(2013\)](#), we must take into account the per-band mean differences between DR7 and DR15.
- One CALSPEC star (BD+17°4708) is now a suspected variable star ([Bohlin & Landolt 2015](#); [Marinoni et al. 2016](#)). We thus exclude it, as in the rest of this work. Another CALSPEC star (P041C, a G0V star) has a discovered M dwarf companion (). We exclude it from the  $i$  and  $z$  calibrations, where the companion flux has an impact at the  $\sim 1\%$  level. As in [Betoule et al. \(2013\)](#), we exclude the hot white dwarf stars (GD71, G191B2B, GD153) from the  $u$ -band calibration, as they have uncertain transformations between the PT and the main SDSS telescope.
- CALSPEC has been updated through several versions; as in the rest of this work, we use the September 2019 CALSPEC version.

We use the following nomenclature to describe these different magnitudes (where the magnitude  $m$  can be  $u$ ,  $g$ ,  $r$ ,  $i$ , or  $z$ ): are the SDSS DR7 magnitudes with no AB offsets applied;  $m_{\text{SDSS DR7}}^{\text{AB13}}$  are SDSS DR7 magnitudes with the [Betoule et al. \(2013\)](#) AB offsets applied;  $m_{\text{SDSS DR7}}^{\text{AB}}$  are SDSS DR 7 magnitudes with the above updates; finally are DR15 PSF magnitudes with no AB offsets. Our goal is to compute new offsets for DR15 as follows:

$$m_{\text{SDSS DR15}} - m_{\text{SDSS DR7}}^{\text{AB}} \quad (\text{C1})$$

$$= [m_{\text{SDSS DR15}} - m_{\text{SDSS DR7}}^{\text{AB13}}] \quad (\text{C2})$$

$$+ [m_{\text{SDSS DR7}} - m_{\text{SDSS DR7}}^{\text{AB}}] \quad (\text{C3})$$

$$+ [m_{\text{SDSS DR7}}^{\text{AB13}} - m_{\text{SDSS DR7}}] \quad (\text{C4})$$

Each term in the sum is given as columns in [Table 5](#). To obtain the first term ([Equation C2](#)), we take the [Betoule et al. \(2013\)](#) SDSS tertiary catalog and match 2,000 randomly selected stars against DR15, finding the median offsets. For the

second term ([Equation C3](#)), we compute the offset between synthetic photometry and the PT CALSPEC observations (transformed into the SDSS DR7 system). [Table 6](#) presents this process. Finally, the last term is taken from [Betoule et al. \(2013\)](#) and [Sako et al. \(2018\)](#).

CALSPEC Star	$g_{\text{PS1, Ap}}$	$g_{\text{PS1, Syn}}$	Difference	$r_{\text{PS1, Ap}}$	$r_{\text{PS1, Syn}}$	Difference	$i_{\text{PS1, Ap}}$	$i_{\text{PS1, Syn}}$	Difference
vb8_stiswfcnic_001	17.4172	17.4477	...	16.0360	15.9995	...	13.2413	13.2387	0.0025
hs2027_stis_004	16.4668	16.4689	-0.0021	16.8404	16.8384	0.0020	17.2156	17.1999	0.0157
sf1615_001a_stisnic_007	16.9843	16.9821	0.0022	16.5566	16.5561	0.0005	16.3868	16.3825	0.0043
c26202_stiswfcnic_001	16.6621	16.6659	-0.0038	16.3483	16.3623	-0.0140	16.2502	16.2652	-0.0150
snap2_stiswfcnic_001	16.4316	16.4343	-0.0027	16.0508	16.0403	0.0105	15.9078	15.9073	0.0005
wd1657_343_stiswfcnic_001	16.2152	16.2311	-0.0159	16.7013	16.6945	0.0068	17.0761	17.0753	0.0008
snap1_stisnic_006	15.4912	15.5010	-0.0098	15.8912	15.8951	-0.0039	16.2036	16.2020	0.0016
lds749b_stisnic_006	14.5828	14.5745	0.0083	14.7983	14.8088	-0.0104	15.0280	15.0381	-0.0101
kf06t2_stiswfcnic_001	14.4139	14.4039	0.0100	13.6002	13.6011	-0.0009	...	...	...
p177d_stisnic_007	13.6756	13.6896	-0.0140	...	...	...	...	...	...
gd153_stiswfcnic_001	13.1146	13.1324	-0.0178	13.5858	13.5935	-0.0077	13.9678	13.9742	-0.0064
kf08t3_stisnic_001	13.6593	13.6546	0.0046	...	...	...	...	...	...
gd71_stiswfcnic_001	12.8458	12.8272	0.0186	13.2839	13.2717	0.0122	13.6285	13.6435	-0.0150
Average	...	...	-0.0019	...	...	-0.0005	...	...	-0.0021
RMS	...	...	0.0112	...	...	0.0087	...	...	0.0134

**Table 4.** PSF photometry and synthetic (AB magnitude) photometry for  $g_{\text{PS1}}$ ,  $r_{\text{PS1}}$ , and  $i_{\text{PS1}}$  for CALSPEC stars observed by Pan-STARRS1. The average difference for each filter is the new AB offset, in the sense that subtracting these values from the Pan-STARRS1 aperture magnitudes brings them onto the AB system as measured by CALSPEC. VB8 is a possible outlier in  $g_{\text{PS1}}$  and  $r_{\text{PS1}}$ , so we exclude it.

SDSS Filter	$m_{\text{SDSS DR15}} - m_{\text{SDSS DR7}}^{\text{AB13}}$	$m_{\text{SDSS DR7}} - m_{\text{SDSS DR7}}^{\text{AB}}$	$m_{\text{SDSS DR7}}^{\text{AB13}} - m_{\text{SDSS DR7}}$	$m_{\text{SDSS DR15}} - m_{\text{SDSS DR7}}^{\text{AB}}$
<i>u</i>	+0.070	+0.0710	-0.0679	+0.073
<i>g</i>	-0.014	-0.0277	0.0203	-0.021
<i>r</i>	-0.002	-0.0158	0.0049	-0.013
<i>i</i>	-0.015	-0.0283	0.0178	-0.025
<i>z</i>	-0.013	-0.0198	0.0102	-0.023

**Table 5.** Computing updated AB offsets for SDSS DR15. Appendix C describes the terms; the last column is the sum of the first three and is the final SDSS DR15 AB offset.

Star	<i>u</i>	<i>g</i>	<i>r</i>	<i>i</i>	<i>z</i>
Transformed from PT by <a href="#">Betoule et al. (2013)</a>					
G191B2B	11.048	11.456	12.014	12.388	12.735
GD153	12.699	13.051	13.573	13.936	14.289
GD71	12.429	12.736	13.236	13.597	13.946
P041C	13.569	12.261	11.844	11.716	11.707
P177D	15.118	13.743	13.299	13.157	13.128
P330E	14.553	13.28	12.839	12.697	12.675
BD+17°4708	10.56	9.631	9.352	9.245	9.241
Synthetic CALSPEC Photometry					
g191b2b_stiswfcnic_001	11.0072	11.4760	12.0199	12.4094	12.7577
gd153_stiswfcnic_001	12.6772	13.0748	13.5869	13.9639	14.3058
gd71_stiswfcnic_001	12.4347	12.7750	13.2655	13.6335	13.9706
p041c_stisnic_007	13.5030	12.2866	11.8618	11.7585	11.7439
p177d_stisnic_007	15.0505	13.7791	13.3168	13.1888	13.1517
p330e_stiswfcnic_001	14.4734	13.3019	12.8491	12.7208	12.6862
bd_17d4708_stisnic_006	10.4961	9.6513	9.3613	9.2707	9.2543
Offsets					
G191B2B	...	-0.0200	-0.0059	-0.0214	-0.0227
GD153	...	-0.0238	-0.0139	-0.0279	-0.0168
GD71	...	-0.0390	-0.0295	-0.0365	-0.0246
P041C	0.0660	-0.0256	-0.0178	...	...
P177D	0.0675	-0.0361	-0.0178	-0.0318	-0.0237
P330E	0.0796	-0.0219	-0.0101	-0.0238	-0.0112
BD+17°4708	...	...	...	...	...
Mean	0.0710	-0.0277	-0.0158	-0.0283	-0.0198

**Table 6.** Computing updated AB offsets for SDSS DR7. Each column presents magnitudes for a filter; each row presents magnitudes for a star. The top rows are PT measurements of CALSPEC stars transformed to the SDSS 2.5m by [Betoule et al. \(2014\)](#). The middle rows are synthetic photometry from the latest (September 2019) CALSPEC. The bottom rows show the difference and the mean. As discussed in Appendix C, we exclude BD+17°4708 as a possible variable, we exclude the three WDs from *u* as they cannot be transformed reliably from the PT, and we exclude P041C from the *i* and *z* as it has significant flux in the red from a companion star.